Mechanical Implications of Creep and Partial Coupling on the World's Fastest Slipping Low-angle Normal Fault in Southeastern Papua New Guinea

James Biemiller[1], Carolyn Boulton[2], Laura Wallace[1,3], Susan Ellis[3], Timothy Little[2], Marcel Mizera[2,4], Andre Niemeijer[4], Luc Lavier[1]

[1] Institute for Geophysics, Jackson School of Geosciences, University of Texas at Austin, Austin, Texas, USA.

[2] School of Geography, Environment and Earth Sciences, Victoria University of Wellington, Wellington, New Zealand.

[3] GNS Science, Lower Hutt, New Zealand.

[4] Faculty of Geosciences, Utrecht University, Utrecht, The Netherlands.

Corresponding author: James Biemiller (james.biemiller@utexas.edu)

Key Points:

- GPS velocities reveal horizontal extension of 8.3±1.2 mm/yr (~8-11 mm/yr dip-slip) on a low-angle normal fault dipping ≤24° at the surface
- Shallowest gouges of this fault are frictionally weak and velocity-strengthening; deeper fault rocks are stronger and velocity-weakening
- Fault locking at ~5-16 km depth with shallower and deeper interseismic creep inferred from geologic, experimental, and geodetic results

Abstract (<250 words)

We use densely spaced campaign GPS observations and laboratory friction experiments on fault rocks from one of the world's most rapidly slipping low-angle normal faults, the Mai'iu fault in Papua New Guinea, to investigate the nature of interseismic deformation on active low-angle normal faults. GPS velocities reveal 8.3±1.2 mm/yr of horizontal extension across the Mai'iu fault, and are fit well by dislocation models with shallow fault locking (above 2 km depth), or by deeper locking (from ~5-16 km depth) together with shallower creep. Laboratory friction experiments show that gouges from the shallowest portion of the fault zone are predominantly weak and velocity-strengthening, while fault rocks deformed at greater depths are stronger and velocity-weakening. Evaluating the geodetic and friction results together with geophysical and microstructural evidence for mixed-mode seismic and aseismic slip at depth, we find that the Mai'iu fault is most likely strongly locked at depths of ~5-16 km and creeping updip and downdip of this region. Our results suggest that the Mai'iu fault and other active low-angle normal faults can slip in large ($M_w > 7$) earthquakes despite near-surface interseismic creep on frictionally stable clay-rich gouges.

Plain Language Summary

In regions of extension, where tectonic plates pull apart, the Earth's crust breaks along fractures, or 'normal faults,' that allow parts of the crust to slip past each other. Many of these faults intersect the Earth's surface at a steep angle, but some anomalously low-angle normal faults are oriented at a shallower angle to the surface. Faults can slip during infrequent fast earthquakes or through slower gradual fault creep. Because active low-angle normal faults are rare and typically have low long-term slip-rates, it is not clear whether they cause large earthquakes or creep gradually. Using two approaches, this study addresses whether earthquakes occur on one of the fastest-slipping of these types of faults, the Mai'iu fault in Papua New Guinea. One approach uses GPS measurements to track patterns of displacement of the Earth's surface near the Mai'iu fault over three years. Surface displacements confirm that the Mai'iu fault slips actively and are used to constrain models of fault slip at depth. The second approach uses laboratory experiments on rocks from the Mai'iu fault zone to test whether these rocks tend to slip unstably in earthquakes, or creep stably under conditions similar to those in the fault zone. Laboratory results show that rocks from the shallowest parts of the fault tend to creep stably, while deeper fault rocks tend to slip unstably. Combining

laboratory, geological and GPS results to map slip behaviors to different fault zone depths, we find that the Mai'iu fault most likely creeps near the Earth's surface but can generate larger earthquakes at greater depths.

1.1. Introduction

Active continental rift systems accommodate extension at rates ranging from <1 mm/yr to a few cm/yr (Abers, 2001; Ruppel, 1995). This extension is facilitated by a variety of seismic and aseismic deformation processes on normal faults, including slip in devastating M_w 6+ earthquakes such as the 6 April 2009 L'Aquila event in Italy that killed over 300 people (Anzidei et al., 2009). Some extending regions, such as the Gulf of Corinth and the Apennines, experience frequent earthquakes on steeply dipping (>40°) near-surface fault sections (Abers, 2009; Jackson, 1987; Jackson & McKenzie, 1983). In these same systems, there is also evidence for aseismic creep on other, less steeply-dipping normal faults (Abers, 2009; Hreinsdóttir & Bennett, 2009; Valoroso et al., 2017). Extensional systems commonly consist of a series of near-surface high-angle (dipping 40-70°) normal faults that are at least in part seismogenic, and that sole into a deeper low-angle (<30°) to sub-horizontal detachment fault, which may creep aseismically (Abers, 2009; Collettini, 2011; Wernicke, 1995).

The mechanics of initiation and subsequent slip of detachment faults dipping at low angles (<30°) near the Earth's surface are not fully understood. These 'low-angle normal faults' (LANFs) appear to defy Mohr-Coulomb friction theory. This theory posits that under a vertical maximum principal stress, normal faults formed in the brittle crust with Byerlee values of friction should initiate at dips of 60-70° and should frictionally lock up and stop slipping at dips <30° (e.g., Axen, 1992, 2004; Wernicke, 1995). However, geologic offsets of ~10 km or more on shallowly dipping detachments are commonly observed globally (e.g., Wernicke, 1995; Collettini, 2011; Platt et al., 2015), and a variety of seismological, geodetic and geologic observations indicate that some LANFs are active today (e.g., Abers, 2001, 2009; Anderlini et al., 2016; Chiaraluce et al., 2007, 2014; Collettini, 2011; Hreinsdóttir & Bennett, 2009; Numelin et al., 2007a; Valoroso et al., 2017; Wallace et al., 2014; Webber et al., 2018). Dip slip rates of active and inactive LANFs range from <1 to 10s of mm/yr (Webber et al., 2018). The mechanical paradox of slip on LANFs is most apparent at or near the Earth's surface, where the maximum principal stress is likely to be near-

93 vertical and deformation is assumed to occur predominantly by brittle, frictional failure (e.g.,
94 Abers, 2009).
95 A longstanding and societally important question is whether LANFs can generate large
96 earthquakes and, if so, how frequently (e.g., Wernicke, 1995). The instrumental record of M_w >
97 5.5 normal-fault earthquakes with unambiguously discriminated rupture planes is sparse
98 (Collettini et al., 2019; Jackson & White, 1989), but it includes two events in the Gulf of Corinth
99 with reported dips as low as 30° and 33°, and with magnitudes of 5.9 and 6.2, respectively. Other
100 earthquakes with indiscriminate nodal planes are inferred to reflect LANF slip based on their
101 seismological and geological context (Collettini, 2011), including the notable 29 October 1985 M_w
102 6.8 Woodlark Basin earthquake. This event occurred around a seismologically imaged LANF,
103 aligned parallel to one of the focal planes, and may be the largest LANF earthquake documented
104 globally (Abers, 2001; Abers et al., 1997).
105 Due to the rarity and typically low slip rates (a few mm/yr or less) of active LANFs (Webber
106 et al., 2018), geodetic observations across them are scarce and can be difficult to interpret.
107 However, available results indicate some degree of aseismic creep on the active Altotiberina
108 LANF in the Northern Appenines, Italy (Anderlini et al., 2016; Chiaraluce et al., 2014; Hreinsdóttir
109 & Bennett, 2009; Valoroso et al., 2017). GPS velocities have been used to infer that this fault
110 actively slips at 1.5 mm/yr (Anderlini et al., 2016) to 2.4 mm/yr (Hreinsdóttir & Bennett, 2009).
111 Slip on the Altotiberina fault occurs either by partial creep on a fault that is heterogeneously
112 coupled in space (Anderlini et al., 2016), or by aseismic creep below a locking depth of 4 km
113 (Hreinsdóttir & Bennett, 2009).
114 A variety of mechanisms have been proposed for aseismic creep on LANFs. These include:
115 1) an enhanced tendency for stable slip resulting from elevated pore-fluid pressures (Axen, 1992;
116 Collettini & Barchi, 2004; Ikari et al., 2009; Abers, 2009); 2) rotated principal stress orientations
117 favoring slip on low-angle faults (Axen, 1992, 2019); and/or 3) creep on interconnected networks
118 of frictionally stable minerals (e.g., Collettini, 2011; Collettini et al., 2019) such as talc (Collettini
119 et al., 2009a), clays (Ikari et al., 2009; Ikari & Kopf, 2017) or serpentine (antigorite/lizardite)
120 (Floyd et al., 2001). It remains unclear whether fault rocks composed of these frictionally stable
121 mineralogies are abundant on active LANFs; and, in particular, whether they are present (or
122 thermodynamically stable) at the depths where LANFs are inferred to be creeping. One promising
123 approach to understanding mechanisms of LANF slip involves the integration of friction

experiments and microstructural analyses of rocks exhumed along an active LANF with corresponding geodetic observations of surface deformation around the same fault. Such an integrated approach has the potential to illuminate the mechanics and spatial extent of active LANF slip. Evaluating these disparate datasets in tandem can help connect geodetic signals of LANF slip to geologically and experimentally constrained deformation mechanisms.

Here, we address the question of whether LANFs creep aseismically or slip in earthquakes following periods of locking and interseismic elastic strain accumulation by presenting and modeling data from a dense campaign GPS network spanning the world's most rapidly slipping active LANF, the Mai'iu fault in southeast Papua New Guinea (PNG; Webber et al., 2018). To strengthen our interpretation of the geodetic data, we perform hydrothermal velocity-stepping friction experiments on exhumed samples from different parts of the Mai'iu fault rock sequence under a range of relevant crustal conditions. Our results complement new microstructural observations of deformation mechanisms within the Mai'iu fault rocks in Mizera et al. (submitted). Geological and geodetic evidence suggests that the Mai'iu fault slips at dip-slip rates of ~10 mm/yr (Wallace et al., 2014; Webber et al., 2018). The Mai'iu fault is therefore an ideal natural laboratory in which to use both geology and geodesy to study the nature of interseismic deformation on an active crustal-scale, misoriented fault. We employ detailed geodetic surveys, elastic dislocation modelling techniques, and laboratory friction experiments on rocks from the Mai'iu fault to address the mechanics and seismic behavior of a rapidly slipping, active LANF.

1.2. Tectonic and geological setting of the Mai'iu fault

The Woodlark Rift in southeast PNG is a young, actively propagating rift located within a region of microplates between the converging Pacific and Australian plates (Figure 1a; Baldwin et al., 2012 and references within) and is well-known for hosting active low-angle normal faults near its westward transition from oceanic spreading to continental rifting (Abers, 1991, 2001; Abers et al., 1997, 2016; Little et al., 2007). Northward subduction of Solomon Sea oceanic lithosphere at the San Cristobal and New Britain trenches drives rapid counterclockwise rotation of the Woodlark and Trobriand microplates at 2–2.7°/Myr relative to Australia about nearby Euler poles to the SW (Figure 1a), yielding primarily N-S extension in the Woodlark Rift. Extension rates range from 20–35 mm/yr in the eastern Woodlark spreading center to 5–15 mm/yr in the onshore continental portion of the rift in the Papuan Peninsula and D'Entrecasteaux Islands

(Wallace et al., 2014). Recent seismicity is focused just west of the oceanic-continental rift transition, following the Woodlark Rise westward through the D'Entrecasteaux Islands (Abers et al., 1997, 2016). This seismicity commonly aligns with geologically mapped and/or geodetically inferred active normal faults or strike-slip transfer faults (Little et al., 2007, 2011; Wallace et al., 2014). From Goodenough Island west to Cape Vogel, microseismicity focused in the upper 15 km along a WSW-trending corridor termed the Ward Hunt Strait fault zone delineates a possible actively deforming transfer zone in continental crust near the Papuan Peninsula (Abers et al., 2016; Figure 1b). Few shallow (<12 km) earthquakes have been observed to the west of the Ward Hunt Strait fault zone, where most extension appears to collapse onto a single fault—the low-angle Mai'iu fault. Offshore to the northeast of the Mai'iu fault trace, aligned microseismicity from 12-25 km depth outlines a 30-40°-dipping planar zone inferred to be the downdip extent of the Mai'iu fault (Abers et al., 2016).

Dipping ~21° where it intersects the Earth's surface, the Mai'iu fault is the dominant mapped fault in the continental Woodlark rift between 149.0–149.6°E (Figure 1; Abers et al., 2016; Mizera et al., 2019; Little et al., 2019; Wallace et al., 2014). The footwall of the Mai'iu fault hosts the actively exhuming Dayman-Suckling metamorphic core complex, a smoothly corrugated domal structure exposing very low-grade (pumpellyite-actinolite-facies) rocks near its ~3 km-high crest and higher-temperature (greenschist-facies) rocks along its northern margin near sea level (Daczko et al., 2009; Little et al., 2019). The Mai'iu fault juxtaposes metabasaltic rocks—the Goropu Metabasalt—in its footwall against ultramafic rocks of the Papuan Ultramafic Belt, and structurally above, unmetamorphosed conglomeratic rocks in its hanging wall (e.g., Little et al., 2019; Mizera et al., submitted). Over the past few Myr, the Mai'iu fault is inferred to have slipped at ~12 mm/yr, based on the slip-parallel width (at least 30 km) of exhumed fault remnants atop the Dayman-Suckling metamorphic core complex and the exposure at >2 km elevation of 2–3 Ma syn-extensional granites in the footwall that were originally buried at depths of 4–10 km (Little et al., 2019; Mizera et al., 2019; Österle et al., 2020). In addition, accumulation of cosmogenic nuclides in quartz veins on the exhumed fault scarp of the Mai'iu fault indicate Holocene to present-day dip-slip rates of 11.7±3.5 mm/yr (Webber et al., 2018). For a 21° dip, modern dip-slip rates of 7.5–9.6 mm/yr across the Mai'iu fault have been estimated from a regional-scale network of GPS velocities (Wallace et al., 2014) and agree well with geologic slip rates.

185 Minor synthetic and antithetic splay faults in the hanging wall of the Mai'iu fault are presumed
186 to intersect the active fault at depths of up to a few km (Figure 1; Little et al., 2019; Mizera et al.,
187 2019). The most prominent of these, the Gwoira fault, cuts the upper ~1 km of the Mai'iu fault
188 hanging wall east of Mt. Dayman (Webber et al., 2020). Inception of this splay fault led to
189 abandonment of the shallowest portion of the Mai'iu fault farther south. East of the Gwoira fault,
190 the Mai'iu fault system steps offshore and remains active along the southern Goodenough Bay
191 coastline, as evidenced by Holocene uplift of coral reef terraces at rates of up to 4.3 mm/yr
192 (Biemiller et al., 2018; Mann & Taylor, 2002; Mann et al., 2009). The well-preserved platform-
193 notch-platform morphology and clustered $^{230}Th/^{234}U$ ages of these emerged reefs reflect episodic
194 and presumably coseismic meter-scale uplift events, suggesting that the Goodenough Bay segment
195 of the Mai'iu fault system slips in moderately large ($M_w > 7$) earthquakes (Biemiller et al., 2018).
196

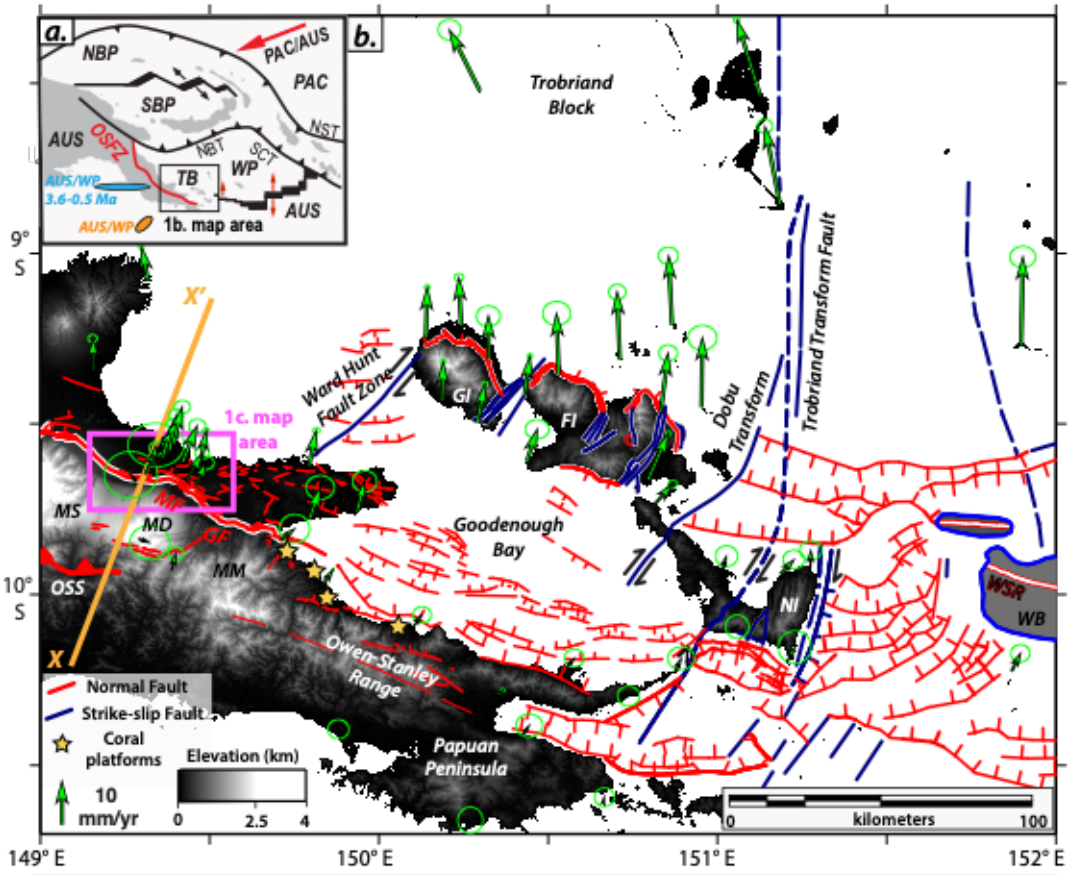
a.
NBP
PAC/AUS
PAC
SBP
NST
AUS
OSFZ
NBT
SCT
WP
TB
AUS/WP
3.6-0.5 Ma
AUS/WP
AUS
1b. map area
b.
Trobriand Block
Ward Hunt Fault Zone
GI
FI
Dobu Transform
Trobriand Transform Fault
1c. map area
MS
MD
GF
MM
OSS
Goodenough Bay
NI
WSR
WB
Owen Stanley Range
Papuan Peninsula
X'
X
9° S
10° S
Normal Fault
Strike-slip Fault
Coral platforms
10 mm/yr
Elevation (km)
0
2.5
4
0
kilometers
100
149° E
150° E
151° E
152° E

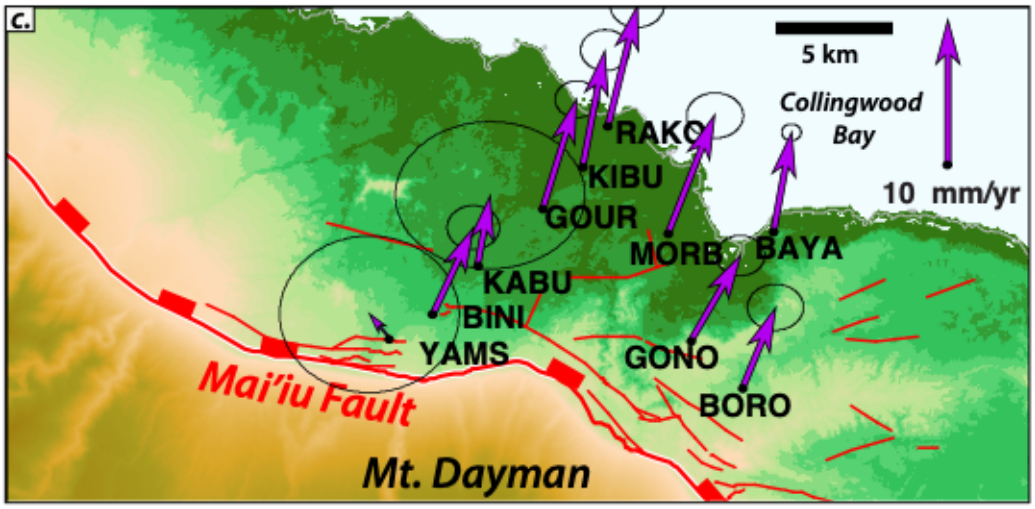
c.
5 km
Collingwood Bay
10 mm/yr
RAKO
KIBU
GOUR
MORB
BAYA
KABU
BINI
YAMS
GONO
BORO
Mai'iu Fault
Mt. Dayman

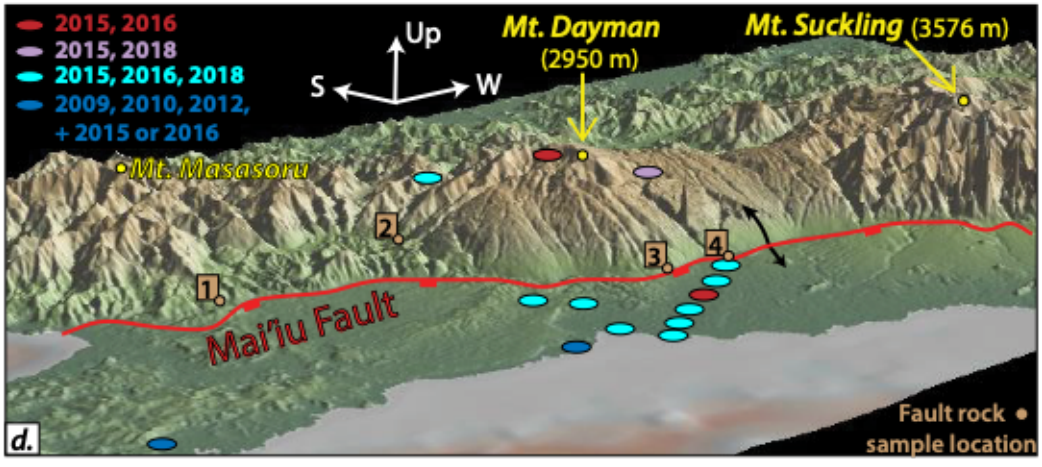
2015, 2016
2015, 2018
2015, 2016, 2018
2009, 2010, 2012, + 2015 or 2016
Up
S
W
Mt. Dayman (2950 m)
Mt. Suckling (3576 m)
Mt. Masasoru
1
2
3
4
Mai'iu Fault
Fault rock sample location
d.

198 **Figure 1.** a.) Regional tectonic map of PNG with main map area outlined, showing overall
199 Australia-Pacific Plate convergence and Woodlark spreading (vectors). Ellipses show modern
200 (orange; Wallace et al., 2014) and 3.6–0.5 Ma (cyan; Taylor et al., 1999) poles of rotation of the
201 Woodlark Plate relative to the Australian Plate. b.) Topographic map with faults from Little et al.
202 (2007, 2011, 2019) and GPS velocities relative to the Australian Plate (section 2; Wallace et al.,
203 2014). Ellipses show 95% confidence intervals based on formal uncertainties. Stars indicate
204 uplifted Holocene coral platforms. Dashed box shows area of 1c. c.) Enlarged map of dense GPS
205 velocity field on the Mai'iu fault hanging wall. d.) Oblique view of the Mai'iu fault and Dayman-
206 Suckling Metamorphic Core Complex (Mt. Masasoru, Mt. Dayman, and Mt. Suckling). Black
207 arrows show sense of motion across the fault. Ellipse colors show observation years at GPS sites
208 near the fault (see key), and brown circles show fault rock sample locations. Samples from each
209 site include: 1.) PNG-15-70; 2.) PNG-14-19E, PNG-14-19F, and PNG-16-17D2H; 3.) PNG-14-
210 33A and PNG-14-33B; 4.) PNG-15-50B and PNG-16-151e from adjacent sites; see Figure S6 for
211 details. Topography from 90-m SRTM (Shuttle Radar Topography Mission) data and GeoMapApp
212 (http://www.geomapapp.org). AUS = Australian Plate; PAC = Pacific Plate; NBP = North
213 Bismarck Plate; SBP = South Bismarck Plate; WP = Woodlark Plate; NBT = New Britain Trench;
214 SCT = San Cristobal Trench. MF = Mai'iu fault; GF = Gwoira fault; MS = Mt. Suckling; MD =
215 Mt. Dayman; MM = Mt. Masasoru; OSS = Owen-Stanley Suture zone; GI = Goodenough Island;
216 FI = Fergusson Island; NI = Normanby Island; TB = Trobriand Block; WSR = Woodlark
217 Spreading Ridge; WB = Woodlark Basin.
218
219

220 **1.3. Mai'iu fault rock sequence and deformation mechanisms**

221 Little et al. (2019) details the exhumed Mai'iu fault rock sequence. Working structurally
222 upwards and towards the most recently formed part of the sequence, this includes: a mafic
223 mylonite zone (1 to several 10s of metres thick), a layer of foliated cataclasite-breccia (<2 m
224 thick), an ultracataclasite layer (~40 cm thick), and mineralogically variable fault gouges
225 immediately below the principal displacement surface of the fault (<20 cm thick; see section 3.1
226 for more details of this sequence). The upwardly narrowing arrangement of progressively lower-
227 temperature fault rocks is interpreted as a time sequence of strain localization, where the higher
228 units are more shallowly-derived and have cannibalized those underlying them (Little et al.,
229 2019).

230 The mylonitic rocks are LS-tectonites that have a strong NNE-trending stretching lineation
231 and normal-sense shear fabrics (Little et al., 2019). Pseudosection modelling of the greenschist-
232 facies mineral assemblage (epidote, actinolite, chlorite, albite, titanite, ±quartz, ±calcite) in the
233 mafic mylonites indicates peak metamorphic conditions of ~425±50°C and 5.9–7.2 kbar, and
234 these rocks are inferred to have been exhumed from ~25±5 km depth (Daczko et al., 2009).
235 Microstructural analyses of the polyphase mafic mineral assemblage indicate that Neogene and

younger shearing in the mylonite zone was accomplished by diffusion-accommodated grain-boundary sliding together with syn-tectonic chlorite precipitation at temperatures >270°C (Little et al., 2019; Mizera et al., submitted). The mylonite zone was overprinted and brittlely reworked into the structurally overlying foliated cataclasites.

The foliated cataclasites host abundant pseudotachylite veins that indicate prior seismic slip on the Mai'iu fault. $^{40}Ar/^{39}Ar$ ages for two samples of such veins are ~2.2 Ma (Little et al., 2019). Given the dip-slip rate of ~10 mm/yr, these ages suggest pseudotachylite formation (i.e., seismic slip) at depths of ~10-12 km (Webber et al., 2018; Little et al., 2019). Mutually cross-cutting pseudotachylite veins, ultramylonite bands, and ductilely sheared calcite extension veins in the foliated cataclasite layer imply mixed-mode seismic and aseismic slip, and have been used to infer a peak in fault strength near the brittle-ductile transition (Little et al., 2019, Mizera et al., submitted). Such a strength peak at ~10-12 km depth approximately coincides with the up-dip end of the corridor of microseismicity that Abers et al. (2016) attribute to the Mai'iu fault at depths of 12-25 km. Gouges comprise the principal slip zone in outcrops. The gouges are not cut by veins or folded by any of the foliations present in the underlying units, suggesting that these gouges formed and slipped during latest stages of deformation in the uppermost few km of the fault zone. Overall, microstructural analyses of the Mai'iu fault rock sequence reveal that the fault zone accommodates shear strain in both seismic slip and aseismic creep via a complex synexhumational series of frictional-viscous deformation mechanisms.

2. Campaign GPS experiment

2.1. GPS data and velocities

In 2015, a network of 12 new campaign GPS monuments was installed near Mt. Dayman, ranging from the domal footwall of the Mai'iu fault northward across the fault trace into the lowlands of the hanging wall and the coast of Collingwood Bay (Figure 1d). The network was designed with densest station spacing in the lowlands to resolve any signal of elastic strain accumulation in the hanging wall of the Mai'iu fault. Stations were installed with station spacings of 3–5 km sub-parallel to fault slip direction (NNE, Figure 1d). We measured all these sites in 2015 and remeasured most of them in 2016 and 2018 using Zephyr geodetic antennas with Trimble 5700 and R7 receivers. Due to the absence of road access in the area, all of the lowland sites were

visited on foot and the high mountain footwall sites were accessed via helicopter and on foot. All observations lasted at least two days, with most lasting three or more. A few of the sites were destroyed over the course of the study: URIA was destroyed between 2015–2016 (after the first measurement), and KABU and DD01 were destroyed between 2016–2018 (after the second measurement). Additionally, we remeasured seven previously established sites (Wallace et al., 2014), extending the time series of these original sites and helping tie the new sites into the pre-existing regional campaign GPS network. We incorporated campaign GPS data collected at 40 sites between 2009–2012 by Wallace et al. (2014), as well as data from a few sites measured by Australian National University prior to 2009. The sites and years of all campaign data are listed in Table S1.

Data were processed and aligned with the global reference frame ITRF14 using the GAMIT and GLOBK software packages (Herring et al., 2015, 2018). We used GAMIT to estimate orbital and rotational parameters, ionospheric and neutral atmospheric delays, and phase ambiguities to solve for the relative positions and covariance matrices of sites in our network. We also accounted for ocean tidal loading (from Onsala Space Observatory, http://holt.oso.chalmers.se/loading/) in the processing. These relative solutions were combined with solutions from global continuous GPS stations using a global Kalman filter, GLOBK, placing tight constraints on the positions of a subset of well-established global IGS network sites in order to tie our site positions into the ITRF14 reference frame. Site velocities were estimated from time series of daily position solutions. Formal uncertainties were augmented to account for random-walk noise (e.g., following approaches used by Beavan et al., 2016; Koulali et al., 2015; Williams et al., 2004; Zhang et al., 1997; see Text S1).

To correct for static coseismic displacements at our sites due to regional large earthquakes (e.g., Banerjee et al., 2005; Tregoning et al., 2013), we used STATIC1D (Pollitz, 1996) to calculate the surface displacement at each site due to static elastic interactions from planar dislocations in a spherical layered half-space with PREM elastic stratification (Dziewonski & Anderson, 1981), representing fault slip in the 2007 M_w 8.1 Solomon Islands earthquake and all M_w 6.9+ earthquakes from 2009 to July 2018 (Hayes, 2017; Lay et al., 2017; Lee et al., 2018; Strasser, 2010; Taylor et al., 2008; U.S. Geological Survey, 2019; Wallace et al., 2015). These regional earthquakes were between 350 and 825 km away from our local network spanning the Mai'iu fault. See Text S2 for details.

298 Relative to a fixed Australian Plate, horizontal velocities for sites on the hanging wall of the
299 Mai'iu fault trend NNE, approximately perpendicular to the fault trace. These velocities generally
300 align with previously reported velocities showing southeast PNG rotating counterclockwise
301 relative to the Australian Plate around a nearby Euler pole (Figures 1, 2; Wallace et al., 2014).
302 Hanging-wall velocities gradually increase with strike-perpendicular distance northwards from the
303 fault trace and show 8.3±1.2 mm/yr of NNE-SSW horizontal extension across the fault,
304 corresponding to 7.6-10.2 mm/yr dip-slip rates for a 21°-dipping fault. One outlier is the hanging
305 wall site nearest to the fault trace, YAMS, which shows subtle NNW motion.
306
307 **2.2. Elastic block and dislocation modeling approaches**
308 We undertake two different approaches to modeling the GPS velocity data to investigate the
309 degree of interseismic coupling and slip rates on the Mai'iu fault. To tie our velocities into a
310 regionally kinematically consistent reference frame, we first use an elastic block modeling
311 approach (similar to Wallace et al., 2014). After establishing a fixed-footwall reference frame
312 using the elastic block model, we use simpler two-dimensional elastic dislocation models to
313 determine the Mai'iu fault properties that best explained the observed surface velocity data (similar
314 to Hreinsdóttir & Bennett, 2009).
315 In the elastic block models, we represent the tectonic deformation responsible for GPS
316 velocities in southeast PNG as the interactions between adjacent elastic crustal blocks, with each
317 rotating about an independent Euler pole of rotation. Although we are most interested in near-field
318 deformation associated with the Mai'iu fault, our wider dataset spans the broader southeast PNG
319 region where crustal deformation can be described by the rotations and interactions between
320 numerous microplates and crustal blocks (Wallace et al., 2014; Figures 1, 2a). Therefore, we model
321 multiple crustal blocks (Figure 2a) and invert the GPS velocities for poles of rotation for each
322 block relative to the Australian Plate (our velocities are in an Australia-fixed reference frame).
323 In these crustal block models, elastic strains accumulated along block boundaries are
324 modeled as backslip on block-bounding faults and parameterized by the kinematic fault coupling
325 ratio, Φ, which describes the fraction of predicted relative plate motion that is accrued as a slip
326 deficit rate. For example, if $\Phi = 0$, the fault is creeping at full plate motion rate, while if $\Phi = 1$,
327 there is no creep in the interseismic period of our GPS measurements and the fault is fully locked.
328 The slip deficit rate is simply the coupling ratio multiplied by the long-term slip rate on the fault

329 from the crustal block motions. We use TDEFNODE (McCaffrey, 2002) to jointly invert for the
330 block poles of rotation and the spatial distribution of Φ on block-bounding faults. The model is
331 constrained by kinematic data including GPS velocities, earthquake slip vectors, and transform
332 fault orientations from throughout the southeast PNG region.

333 Block boundaries and fault geometries are defined on the basis of regional tectonics, field
334 mapping studies, and geophysical constraints such as seismicity. For this model, block and fault
335 geometries are based largely on those of Wallace et al. (2014), although some geometries such as
336 the position and dips of the Mai'iu fault have been updated based on recent field mapping (Little
337 et al., 2019; Mizera et al., 2019; Webber et al., 2018, 2020) and seismological observations (Abers
338 et al., 2016). The statistical significance of various block configurations is tested with an *F*-test for
339 block independence (Figures 2a, S3; Table S5). We utilize our preferred configuration for
340 subsequent models testing fault coupling (Figure 2a).

341 Joint inversion of diverse local and regional kinematic datasets within a block model
342 framework helps to ensure that modeled block rotations and fault coupling are consistent with both
343 regional tectonic motions and local observations. In addition, simple 2-D planar dislocation fault
344 models can provide focused insight into the tradeoffs between slip rate, locking depth, and fault
345 geometry, especially for dense GPS networks that span major active faults. For this reason, we
346 also perform a simple inversion of strike-perpendicular GPS velocities across the Mai'iu fault for
347 fault dip, locking depth, and dip-slip rate using the solutions for planar dislocations in an elastic
348 half-space from Okada (1985). This simplified 2-D approach has been used to model GPS
349 velocities related to slip on other LANFs (Hreinsdóttir & Bennett, 2009) and reverse and strike-
350 slip faults (Beavan et al., 1999). In such models, a single fault is represented as a two-dimensional
351 planar dislocation that extends infinitely in the third dimension. In our case, predicted elastic
352 contributions to surface displacement due to interseismic backslip on the locked dislocations are
353 added to the long-term fault-strike-perpendicular plate motion rate and compared with observed
354 surface velocities to calculate the misfit between the model and the data. By minimizing the data
355 misfit as expressed by the reduced χ^2, these models highlight the range of fault properties and
356 locking most likely responsible for observed surface displacements. The calculated χ^2 is minimized
357 through an extensive grid search of the three fault parameters (dip, slip rate, and locking
358 distribution), as discussed in Section 3.2.
359

360 **2.3. Elastic block model results**

361 Our preferred elastic block model treats Fergusson/Goodenough Islands, Normanby Island,
362 Goodenough Bay, and the Papuan Peninsula as discrete independent crustal blocks, similar to that
363 of Wallace et al. (2014). More complex configurations (with additional blocks) do not produce a
364 statistically significant improvement in fit to the data (see *F*-tests and results in Figures 2a, S3;
365 Table S5). The best-fitting model of jointly inverted block poles of rotation and fault locking are
366 shown in Figure 2a, indicating 8.3±1.2 mm/yr of horizontal extension across the Mai'iu fault. This
367 model predicts locking of the western segment of the Mai'iu fault down to only 2 km depth, below
368 which the fault creeps. Deeper locking occurs on the eastern segment through Goodenough Bay
369 and the faults immediately north of Goodenough Island, although this is not well-constrained due
370 to a relative lack of GPS sites on the largely submarine hanging-wall east of our study area.

371 Inversions producing the model in Figure 2 allow fault coupling ratios to vary from 0 – 1, but
372 they impose a constraint that coupling decreases with increasing depth. To test how such
373 assumptions affect the preferred locking model, additional inversions were performed with
374 different constraints on locking, such as allowing coupling to vary freely with depth or assuming
375 a discrete and uniform locking depth (Text S3; Figure S4). The large misfit of models with
376 prescribed locking depths from the surface to >~2 km confirm that campaign GPS velocities are
377 inconsistent with Mai'iu fault locking from the surface to more than a few kms depth. Inversions
378 with fewer imposed locking constraints, including those in which no downdip decrease in coupling
379 is prescribed (i.e., no assumption that the fault is locked at the surface), all converge on best-fitting
380 models with shallow locking to <2 km depth (Figure S4), compatible with a LANF creeping at
381 most depths.

382

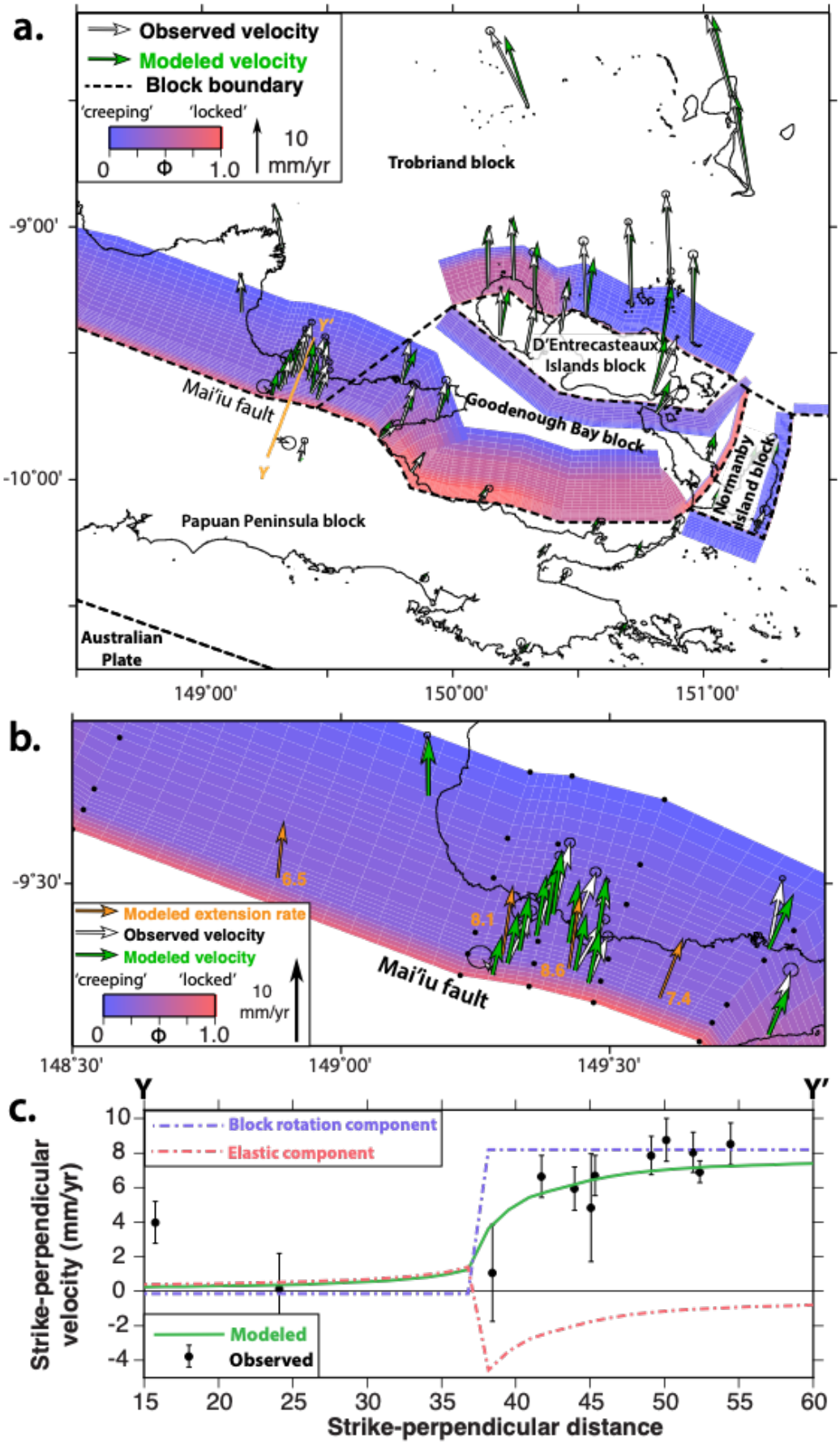
a.
Observed velocity
Modeled velocity
Block boundary
'creeping'
'locked'
0
Φ
1.0
10
mm/yr
Trobriand block
D'Entrecasteaux Islands block
Goodenough Bay block
Normanby Island block
Mai'iu fault
Y
Y'
Papuan Peninsula block
Australian Plate
-9°00'
-10°00'
149°00'
150°00'
151°00'
b.
-9°30'
6.5
8.1
8.6
7.4
Modeled extension rate
Observed velocity
Modeled velocity
'creeping'
'locked'
0
Φ
1.0
10
mm/yr
Mai'iu fault
148°30'
149°00'
149°30'
c.
Y
Y'
Block rotation component
Elastic component
Modeled
Observed
Strike-perpendicular velocity (mm/yr)
Strike-perpendicular distance
10
8
6
4
2
0
-2
-4
15
20
25
30
35
40
45
50
55
60

383

Figure 2. Best-fitting elastic block fault locking model results colored by kinematic fault coupling ratio Φ. Vectors indicate observed (white) and predicted (green) GPS velocities. a.) Preferred locking model. Dashed lines show preferred block boundaries (Figure S3; Table S3). b.) Enlarged view of GPS velocities near the modeled Mai'iu fault, which is predominantly uncoupled below 2 km depth. Labeled orange vectors show modeled rates and directions of relative motion between adjacent blocks across the fault. c.) Strike-perpendicular horizontal velocities relative to the Papuan Peninsula footwall block for sites in the Mai'iu fault network (Profile Y – Y' in 2a). Observed velocities (black), modeled velocities (green), and the modeled velocity contribution of elastic strain (pink) and block rotations (purple) are shown.

2.4. 2-D Dislocation modeling

2.4.1. Model 1: Locked-to-surface models

Modeled crustal block rotations help to establish a footwall-fixed reference frame in which explore Mai'iu fault locking in more detail using 2D dislocation models. We compare the predicted horizontal surface velocities (now in a footwall-fixed reference frame) from 128,000 two-dimensional elastic half-space planar dislocation models to the strike-perpendicular GPS velocities from sites within a 65 km strike-perpendicular distance of the Mai'iu fault trace along profile X-X' (Figure 1b). This approach offers a focused look at how modeled fault properties affect the fit to GPS velocities, but does not account for three-dimensional factors such as along-strike variations in fault geometry or locking. We first test the slip rate, dip angle, and locking depth of a single fault locked to the Earth's surface, as in previous GPS studies of LANF locking (Hreinsdóttir & Bennett, 2009). Although the shallow (≤24°) dip of the Mai'iu fault along its trace is well-constrained (Little et al., 2019; Mizera et al., 2019), the fault surface exhumed on the Dayman-Suckling metamorphic core complex steepens northward (Webber et al., 2020), and fault-related microseismicity implies a similar northward steepening dip (Abers et al., 2016). We therefore allow the modeled fault dip to vary in order to more fully explore the parameter space. We test fault dip angles ranging from 1 - 80° in 1° increments, dip-slip rates of 0.5 – 20 mm/yr in 0.5 mm/yr increments, and locking depths of 0.5 – 20 km in 0.5 km increments (Figures 4a, S6). For the strike-perpendicular horizontal velocities, the best-fitting (minimum $\chi^2 = 0.94$) modeled fault dips 26°, is locked down to 2 km depth, and slips at 10 mm/yr below this depth (model 1; Figure 3a-c). This result indicates that the observed GPS horizontal velocities can be explained by active aseismic creep below a shallow locking depth on a gently dipping normal fault. The close match between the best-fit model's fault dip and the geologically inferred fault dip supports this result. Vertical velocities (which have high uncertainties) are modeled (Figure 3b,e) but not used

419 to constrain the grid search. Joint modeling of vertical and horizontal components (e.g., Beavan et
420 al., 2010; Bennett et al., 2007; Segall, 2010; Serpelloni et al., 2013) yields similar locking results
421 (Text S4). Note that the best-fit $\chi^2 < 1.0$ suggests that the random-walk noise model may slightly
422 overestimate the velocity uncertainty corrections, particularly for campaign sites with only two or
423 three years of observations.
424
425 **2.4.2. Model 2: Consideration of shallow creep and splay fault activity**
426 The setup of model 1 is inherently limited by the assumptions that the fault is locked at the
427 surface and that only one planar structure is active, which may not be appropriate for this and other
428 LANF systems. The hanging walls of major detachment faults are commonly cut by minor splay
429 faults that may variably slip or creep (e.g., Anderlini et al., 2016). In the case of the Mai'iu fault,
430 discontinuous splay faults have been mapped in parts of the hanging wall (Figure 1b; Little et al.,
431 2019, Webber et al., 2020). Additionally, the shallow portions of many LANFs, including the
432 Mai'iu Fault (section 3.2-3.3), contain gouges of weak, frictionally stable mineralogies that may
433 promote near-surface aseismic creep (Collettini, 2011, and references within; Little et al., 2019).
434 To test whether these mechanisms allow aseismic creep in the near-surface portions of the Mai'iu
435 fault and/or its splay faults, we develop buried dislocation models that do not require full fault
436 locking at the Earth's surface and that allow for slip on adjacent splay faults (model 2).
437 Our buried dislocation models allow for creep both updip and downdip of a locked patch
438 or "asperity" (e.g., Collettini et al., 2019). Because the velocity at YAMS is more consistent with
439 footwall motion, we treat it as a footwall site in these models: essentially, this treatment considers
440 the possibility that, in the shallowest subsurface, creep may transfer from the main Mai'iu fault to
441 one of the many active splay faults in the hanging wall, some of which are <1 km from the main
442 fault trace (Little et al., 2019). The modeled fault trace is hence projected between sites YAMS
443 and BINI in order to incorporate YAMS into the footwall. Note that in all dislocation models,
444 including both locked-to-surface and buried dislocation scenarios, the data-fit improves
445 significantly by treating site YAMS as part of the footwall. The best-fit buried dislocation model
446 (model 2; $\chi^2 = 0.89$; Figure 3d-f) fits the horizontal velocities better than the best-fit model with
447 locking imposed at the surface (model 1; $\chi^2 = 0.94$; Figure 3a-c). The best-fit model with a buried
448 locked zone involves a 35°-dipping fault, locked from 5 to 16 km depth and slipping at 10.5 mm/yr
449 updip and downdip of the locked zone (Figure 3d-f), consistent with microseismic, structural, and

surface modeling evidence that the Mai'iu fault steepens to dip 30-40° between ~5-12 km depth (Abers et al., 2016; Little et al., 2019; Webber et al., 2020). Fixing fault dip to a geologically and geodetically reasonable average crustal dip of 35°, Figure 4b shows tradeoffs between the total depth range of locking (depth range D, Figure 3f), the depth of the updip limit of locking (depth P, Figure 3f), and slip rate.

Model 2 assumes that interseismic fault creep updip of a more strongly locked region is mechanically feasible. Shallow interseismic fault creep occurs above locked seismogenic patches on a variety of faults (Harris et al., 2017), including the strike-slip Hayward fault in California (Harris et al., 2017 and references within) and the Nankai subduction megathrust, where periodic slow-slip events near the trench occur updip of the locked portion of the megathrust (Araki et al., 2017). However, recent analytical models predict a strong stress-shadow effect updip of the locked portion of subduction megathrusts that should prevent significant creep on the unlocked updip portion of the fault regardless of its frictional stability (Almeida et al., 2018). In other words, even an unlocked, frictionally stable shallow portion of a megathrust may not feel high enough driving stresses to creep interseismically when located updip of a strongly locked patch. By analogy, this type of model may predict that significant shallow creep updip of a more strongly locked portion of a LANF should not occur, either.

Because the downdip width (~19 km) of the locked LANF patch inferred by model 2 is much smaller than that of a locked megathrust, and because along-strike locking patterns may be heterogeneous and patchy, the efficacy of this stress shadow effect may be limited. Additionally, the stress shadow models (Almeida et al., 2018) assume homogeneous elastic properties at all depths, whereas the shallow portions of many normal fault hanging walls consist of unconsolidated, fractured sedimentary units. High shear stresses associated with deep creep between strong metabasaltic and plutonic rocks could be expected to drive more internal deformation and/or fault creep in weak hanging wall sediments at shallow levels than in the strong hanging wall of the homogeneous model. Heterogeneous locking and elastic properties along with frictionally weak, velocity-strengthening shallow fault gouges (section 3) help explain how shallow interseismic creep coeval with deeper locking (model 2) is a mechanically feasible model for interseismic LANF slip.

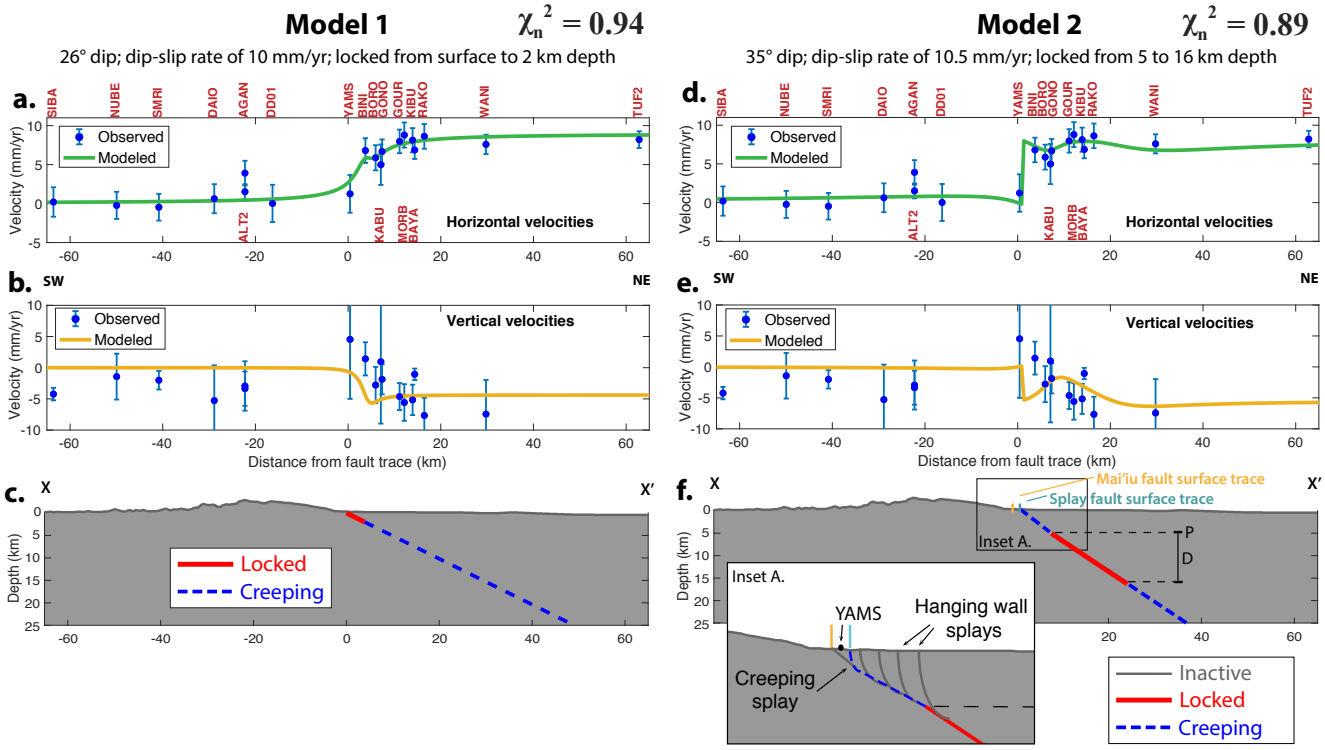

Figure 3. Best-fitting two-dimensional planar elastic half-space dislocation locking models based on strike-perpendicular horizontal velocities projected onto profile X-X' of Figure 1b. Red labels show GPS site names. a-c.) Model 1; locked to 2 km depth. d-f.) Model 2; locked from 5 to 16 km depth, with creep and splay fault slip above 5 km depth. a,d): Observed (blue) and modeled strike-perpendicular velocities. b,e): Observed and modeled vertical velocities. c,f): Schematic of fault locking models. Profile topography from 90-m SRTM data and GeoMapApp (http://www.geomapapp.org).

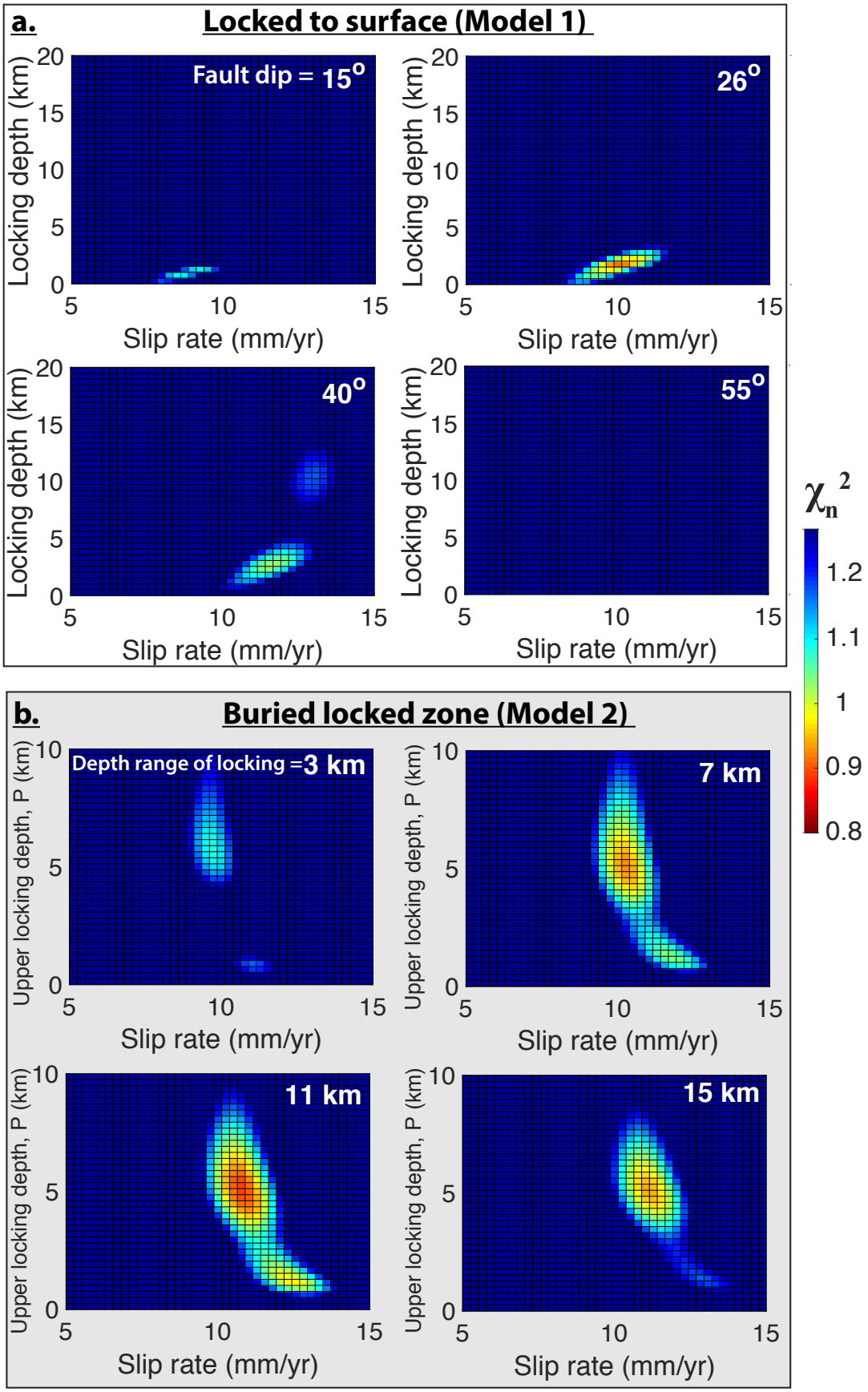
a.
Locked to surface (Model 1)
Fault dip = 15°
26°
40°
55°
Locking depth (km)
Slip rate (mm/yr)
b.
Buried locked zone (Model 2)
Depth range of locking =3 km
7 km
11 km
15 km
Upper locking depth, P (km)
Slip rate (mm/yr)
χn 2
1.2
1.1
1
0.9
0.8

489

Figure 4. Example of misfit (χ^2) tradeoffs for 2D dislocation models capped at χ^2=1.27 (equivalent to 75% confidence interval for model 2 calculated with *F*-tests for statistical significance) to highlight those models that fit the data reasonably well. a.) Tradeoffs between locking depth and slip rate for locked from surface to depth models with different dip angles. Locked-at-surface models prefer shallow locking (<4 km depth) on a shallowly dipping (~26°) fault slipping ~9-12 mm/yr, while steeply dipping faults (≥ 40°) do not fit the data well ($\chi^2 > 1.0$). b.) Buried-dislocation models show tradeoffs between the updip depth of locking (depth P, Figure 3f) and slip rate with different depth ranges of locking (depth D, Figure 3f). Fault dip shown here is fixed to the best-fitting value of 35°; however, P, D, slip rate, and dip were all varied in grid searches. These models prefer a more strongly locked zone from ~5-16 km depth on a shallowly dipping (~35°) fault slipping ~10-12 mm/yr.

3. Mai'iu fault frictional strength and stability from rock deformation experiments

3.1. Fault rock sample descriptions

Over three field seasons, spectacular exposures of the Mai'iu fault were observed and sampled. Structural results show that fault slip has occurred primarily within fault rocks comprising a narrow (< 3 m), high strain fault core (Little et al., 2019) (Figure 5). The frictional properties of these fault rocks likely govern the mode of frictional fault slip at different levels on the fault. Figure 5b shows a schematic section of the Mai'iu fault rock sequence that is partially eroded on exhumed parts of the active fault, but fully preserved in outcrops along the inactive segment of the Mai'iu fault. Eight Mai'iu fault rock samples were studied in detail to determine their mineralogy and frictional properties: two types of footwall foliated cataclasite (Figure 5c); a footwall ultracataclasite (Figure 5d); four types of footwall fault gouge (Figures 5e and 5f); and a sliver of hanging wall serpentine schist entrained within the footwall (Figure 5c, inset).

The mylonitic rocks (not sampled for friction experiments) were overprinted and reworked into the structurally overlying, ~2 m-thick foliated cataclasites. The latter contains veins of friction melt (pseudotachylite), brittle faults, and multiple generations of calcite veins (Figure 5c). The foliated cataclasites investigated in this study (PNG16-17-D2H and PNG16-151E) have a cm-to-mm-spaced, differentiated, and pervasively folded foliation defined by light-coloured albite and quartz±calcite-rich domains and darker phyllosilicate (predominantly chlorite)-rich folia. This microstructure indicates fluid-assisted diffusive mass transfer during the dissolution of mafic minerals (epidote and actinolite) (Mizera et al., submitted). Shear-induced creep by diffusive mass transfer and/or frictional viscous flow likely accompanied the formation and folding of the pervasive foliation (Little et al., 2019; Mizera et al., submitted).

525 In all outcrops, the foliated cataclasites are overlain sharply by a 5-to-40 cm-thick
526 ultracataclasite (PNG15-50B) formed through cataclastic grain-size reduction and authigenic
527 precipitation of calcite, corrensite, and potassium feldspar (Figure 5d). Massive green-gray and
528 red mafic gouges (PNG14-33A and PNG14-33B) or light (PNG14-19E) to medium grey (PNG14-
529 19F) corrensite-saponite gouges sharply overly the ultracataclasite layer and form the <20 cm-
530 thick principal slip zone in surface outcrops (Figures 5a, 5b, 5e and 5f).
531
532

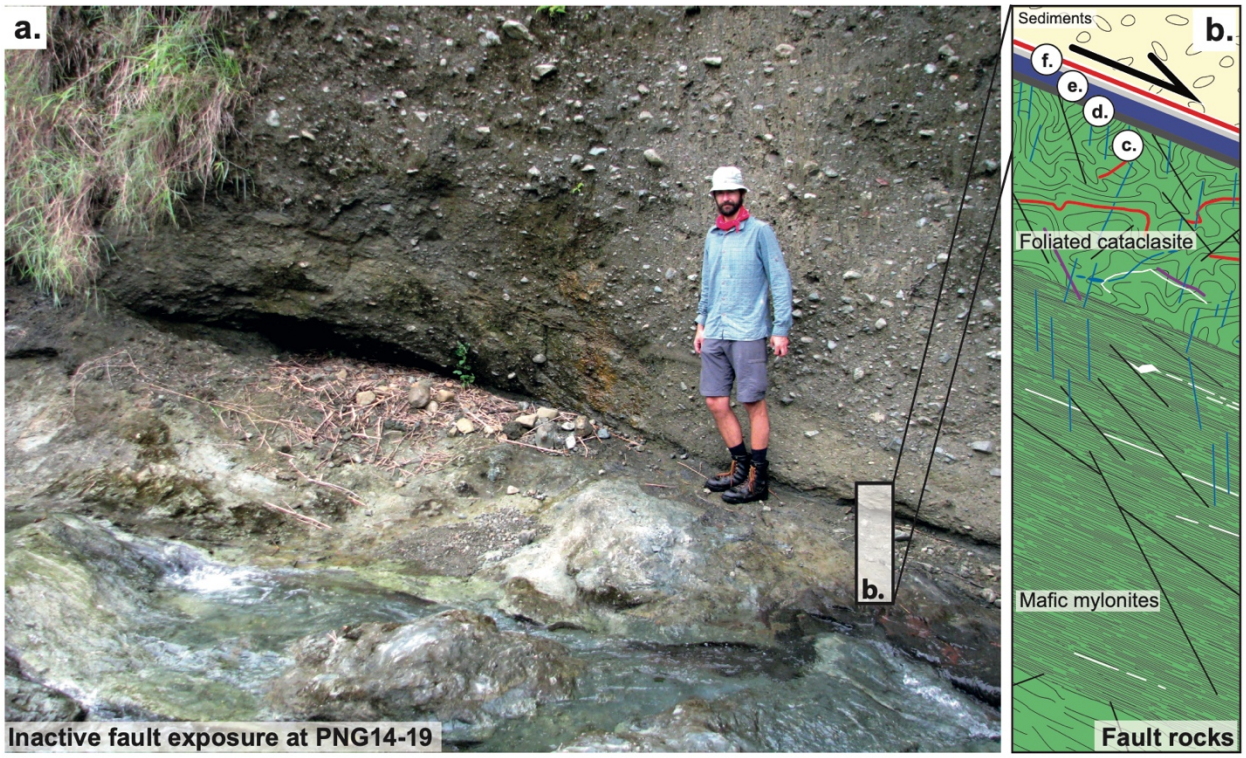
a.
b.
Inactive fault exposure at PNG14-19
Sediments
b.
f.
e.
d.
c.
Foliated cataclasite
Mafic mylonites
Fault rocks

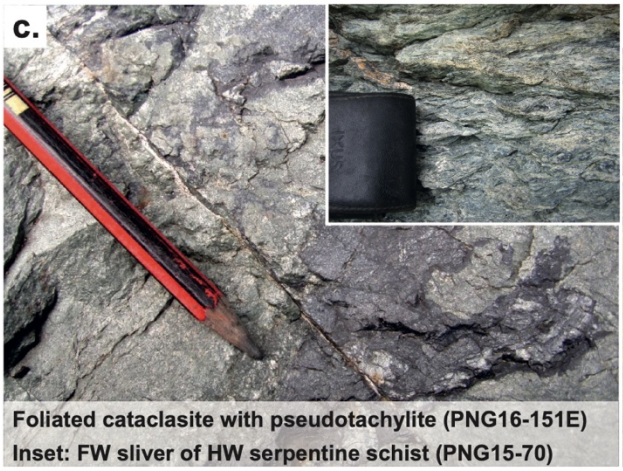
c.
Foliated cataclasite with pseudotachylite (PNG16-151E)
Inset: FW sliver of HW serpentine schist (PNG15-70)


d.
Ultracataclasite (PNG15-50B)

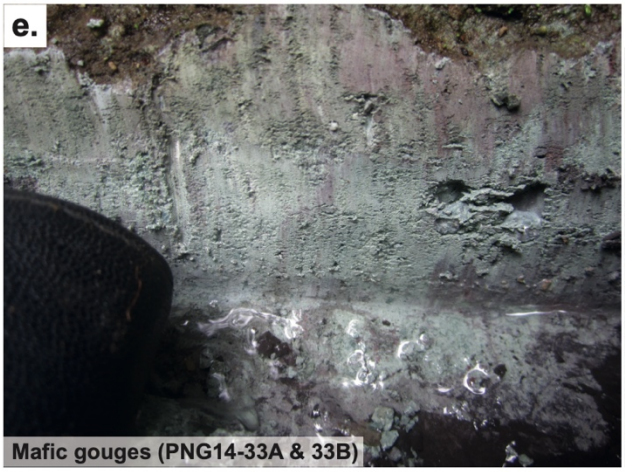
e.
Mafic gouges (PNG14-33A & 33B)


f.
Corrensite-saponite gouge (PNG14-19F)

533

534 **Figure 5.** Summary of fault rocks analyzed. Sample locations are shown in Figures 1d and S7
535 and listed in Table S6. (a) Exposure of the inactive Mai'iu fault showing the footwall fault rock
536 sequence sharply overlain by unmetamorphosed hanging wall sedimentary rocks. (b) A
537 schematic cross section through the fault core, including the structural position of the fault rocks
538 sampled (after Little et al., 2019; Mizera et al., submitted). (c) Fault-exhumed exposure of the
539 foliated cataclasite unit and a pseudotachylite vein. Inset: foliated serpentine schist (>10 m thick)
540 entrained between the footwall and hanging wall of the Mai'iu fault, stranded atop the footwall
541 north of Mt. Masasoru. (d) Outcrop of cohesive ultracataclasite unit structurally overlying
542 foliated cataclasites. (e) Mafic fault gouges, and (f) corrensite-saponite fault gouge comprising
543 the principal slip zone.
544
545

546 **3.2. Experimental methods and materials**

547 We performed hydrothermal friction experiments on powdered gouges derived from eight of
548 these Mai'iu fault rock types (Figure 6; Table S6-7) using the rotary shear apparatus in the High
549 Pressure and Temperature Laboratory at Utrecht University (Niemeijer et al, 2008, 2016). In these
550 experiments, a thin layer (~1.5 mm) of gouge is placed between two ring-shaped Ni-alloy pistons
551 (22/28 mm inside/outside diameter) and confined by Ni-alloy rings with a low friction (Molykote)
552 coating. The piston assembly is mounted inside a water-filled pressure vessel that houses an
553 internal furnace. The vessel is located within a 100 kN capacity Instron loading frame which is
554 used to apply the normal force. Rotation of the vessel creating shear within the layer is achieved
555 using an electromotor attached to two 1:100 gear boxes. For more details, refer to Niemeijer et al
556 (2008, 2016).

557 To create a powdered gouge, samples were crushed and sieved to a grain size fraction < 150
558 μm. In all experiments, we applied stepwise increases in effective normal stress (15 MPa/km),
559 fluid pressure (10 MPa/km) and temperature (25 °C/km) to simulate slip in progressively deeper
560 parts of the fault (Table S5). Once the desired pressure (P) and temperature (T) conditions were
561 reached, we allowed the system to equilibrate for at least 30 minutes before shearing began at 1
562 μm/s. Initial shearing at 1 μm/s occurred for 5 mm to establish a steady state friction level and a
563 mature microstructure. The velocity dependence of friction was investigated by subsequently
564 applying a velocity-stepping scheme of 0.3-1-3-10-30 μm/s. Following these velocity steps, the
565 motor driving displacement was stopped, and PT conditions were changed. Under the new PT-
566 conditions, the 1 μm/s run-in displacement was reduced to 2.5 mm, but otherwise the procedure
567 remained the same. Data were acquired at a rate of 900 Hz and averaged to rates of 1-100 Hz,

568 depending on the sliding velocity. Raw data were processed to obtain shear stress as a function of
569 sliding distance, which was further analyzed in terms of rate-and-state frictional (RSF) properties
570 using a Dieterich state evolution law (Dieterich 1979, 1981; Marone, 1998) and the inversion
571 scheme detailed in Reinen & Weeks (1993) and.
572
573 **3.3. Frictional strength results**
574 We report the results of all experiments in Figure 6, which shows the coefficient of friction
575 (defined as shear stress / effective normal stress, ignoring cohesion) as a function of load-point
576 displacement. All samples tested show changes in friction with PT conditions, but the largest
577 differences in friction are between samples. The measured frictional strength covers the range of
578 μ=0.1 to μ=0.8 (see also Table S7 and Text S5). The uppermost, light gray saponite gouge sample
579 is the weakest with μ=0.11-0.15, followed by the underlying, medium gray saponite gouge
580 (μ=0.18-0.28), the red mafic gouge (μ=0.22-0.35), the serpentinite schist (μ=0.37-0.63), the green-
581 grey mafic gouge (μ=0.40-0.57), the "inactive" foliated cataclasite (0.44-0.75), the "active"
582 foliated cataclasite (μ=0.57-0.67) and finally the ultracataclasite (μ=0.59-0.80). The abundance of
583 the weak clay mineral saponite is a good indicator of the weakness of the sample (e.g. Lockner et
584 al., 2011; Sone et al., 2012), whereas the sample derived from the serpentinite schists show friction
585 values in the range of pure lizardite (e.g. Reinen et al., 1994; Behnsen & Faulkner, 2012). Friction
586 of the foliated cataclasites and the ultracataclasite is comparable to results from friction studies on
587 gouges of granitic composition (e.g. Niemeijer et al., 2016), of quartz (e.g. Chester & Higgs, 1992;
588 Niemeijer et al., 2008), and of plagioclase (e.g. He et al., 2013). In general, the friction coefficients
589 of most fault gouges increase with increasing simulated depth (i.e., increasing temperature,
590 effective normal stress, and fluid pressure) during an individual experiment. In some experiments,
591 strengthening is the result of a long-term displacement-dependent increase in friction (e.g. Figure
592 6c), whereas in other experiments strengthening is abrupt and is the result of increased simulated
593 depth (e.g. Figure 6b).
594

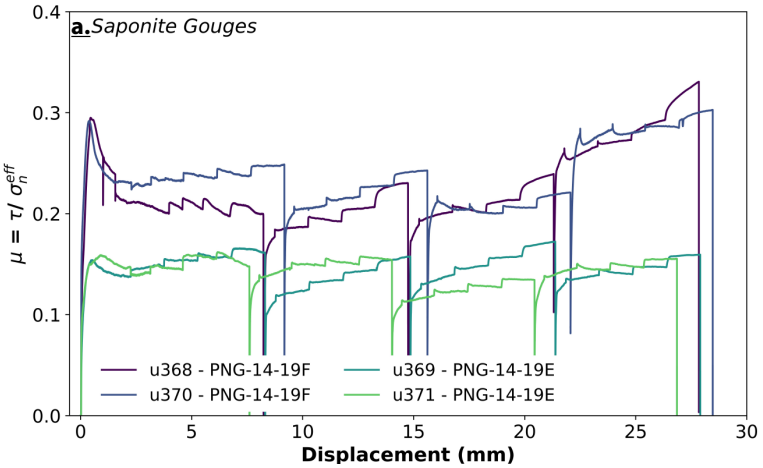
a. Saponite Gouges
u368 - PNG-14-19F
u370 - PNG-14-19F
u369 - PNG-14-19E
u371 - PNG-14-19E
Displacement (mm)

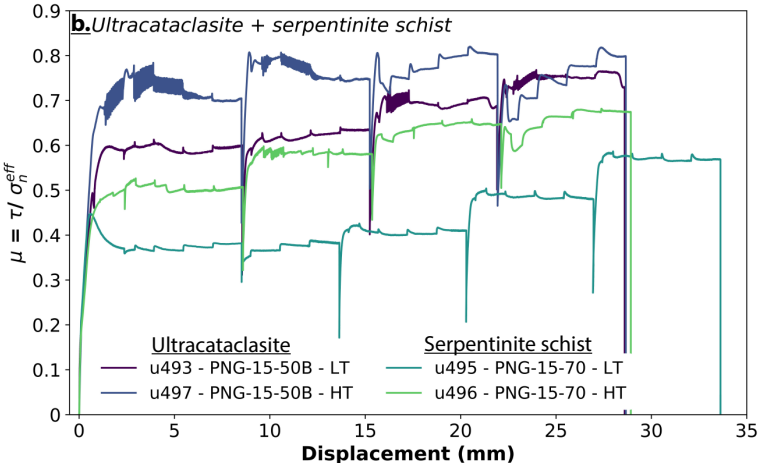
b. Ultracataclasite + serpentinite schist
Ultracataclasite
u493 - PNG-15-50B - LT
u497 - PNG-15-50B - HT
Serpentinite schist
u495 - PNG-15-70 - LT
u496 - PNG-15-70 - HT
Displacement (mm)

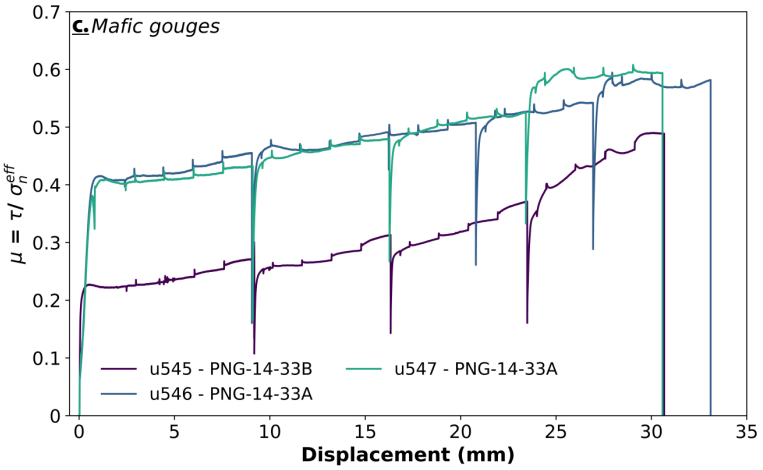
c. Mafic gouges
u545 - PNG-14-33B
u546 - PNG-14-33A
u547 - PNG-14-33A
Displacement (mm)

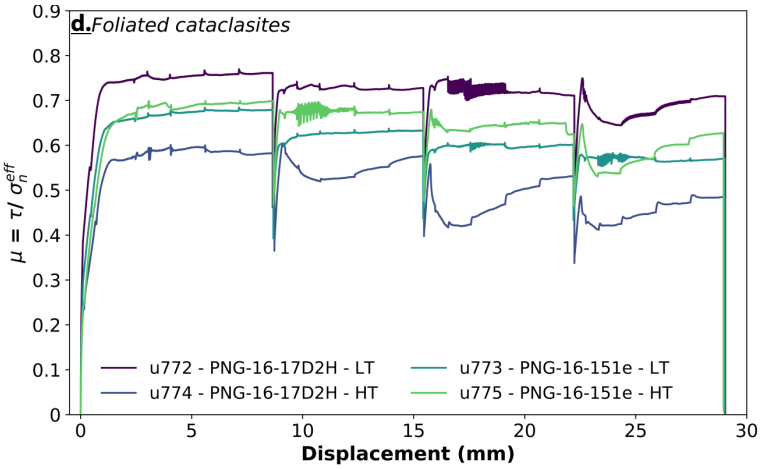
d. Foliated cataclasites
u772 - PNG-16-17D2H - LT
u774 - PNG-16-17D2H - HT
u773 - PNG-16-151e - LT
u775 - PNG-16-151e - HT
Displacement (mm)

595

596 **Figure 6.** Friction measured during velocity-step experiments on Mai'iu fault rocks (Section 3.1,
597 Figure 5, Table S6-7) including a.) corrensite-saponite gouges, b.) ultracataclasite and
598 serpentinite schist; c.) mafic gouges; d.) foliated cataclasites. Colors indicate individual
599 experiments ('u368') on numbered samples ('PNG-14-19F') under lower-temperature (LT) or
600 higher-temperature (HT) conditions.
601

602 **3.4. Rate-and-state frictional stability results**

603 Although a relationship between fault strength and frictional stability has been proposed
604 (Ikari et al., 2011), fault frictional strength alone gives little indication as to whether the fault
605 creeps aseismically or slips in episodic earthquakes. Instead, frictional stability is described
606 within the framework of rate-and-state friction, where the instantaneous effective friction
607 coefficient depends on both the current slip velocity ('rate') and the time over which two fault
608 surfaces have been in contact with each other ('state'). Experimentally derived values of rate-
609 state parameters a, b, and critical slip distance d_c describe the frictional stability of a material:
610 materials with $(a–b)>0$ are velocity-strengthening, whereby an increase in slip velocity causes an
611 increase in friction promoting stable creep; materials with $(a–b)<0$ are velocity-weakening,
612 whereby an increase in slip velocity causes a decrease in friction, promoting unstable, potentially
613 seismic slip (e.g., Dieterich, 1979, 1981; Gu et al., 1984; Rice & Tse, 1986; Ruina, 1983).
614 We invert the velocity-stepping data for individual rate-state friction parameters a, b and d_c.
615 Figure 7 shows $(a–b)$ values as a function of up-step sliding velocity for all samples tested. There
616 is considerable variation in $(a–b)$ with simulated depth. All samples show some negative $(a–b)$
617 values under certain experimental conditions, indicating potential for unstable slip. In all fault
618 gouge-derived samples, $(a–b)$ increases with increasing sliding velocity, regardless of the depth
619 simulated (Figures 7a, 7c). Negative values are restricted to temperatures of 150-200 °C.
620 Samples derived from foliated cataclasites and ultracataclasites show predominantly negative
621 values of $(a–b)$ transitioning to positive values at temperatures of 400 and 450 °C. Interestingly,
622 at these temperatures $(a–b)$ decreases with increasing sliding velocity. Finally, $(a-b)$ values for
623 the sample derived from serpentinite schist show three regimes of velocity dependence, similar
624 to the results of Reinen et al. (1994): low temperature (<200 °C) velocity strengthening,
625 intermediate temperature (200-350 °C) velocity weakening and high temperature velocity
626 strengthening (400-450 °C). As before, $(a–b)$ decreases with increasing sliding velocity in the
627 higher-temperature regime.
628

629

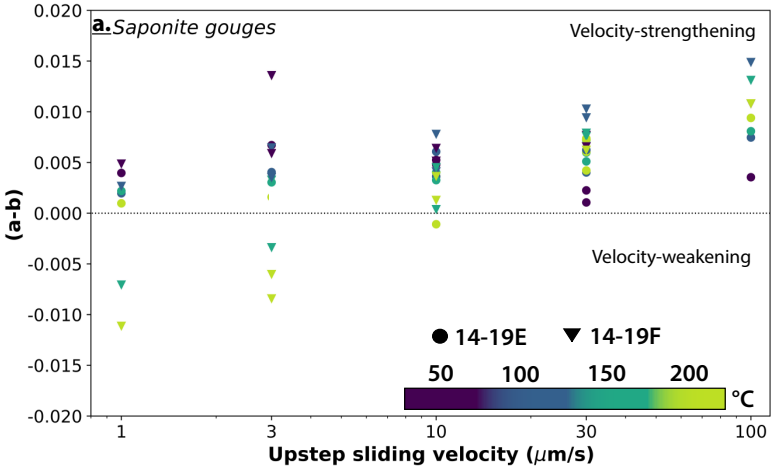
a. Saponite gouges
Velocity-strengthening
Velocity-weakening
14-19E
14-19F
50 100 150 200 °C
(a-b)
Upstep sliding velocity (μm/s)

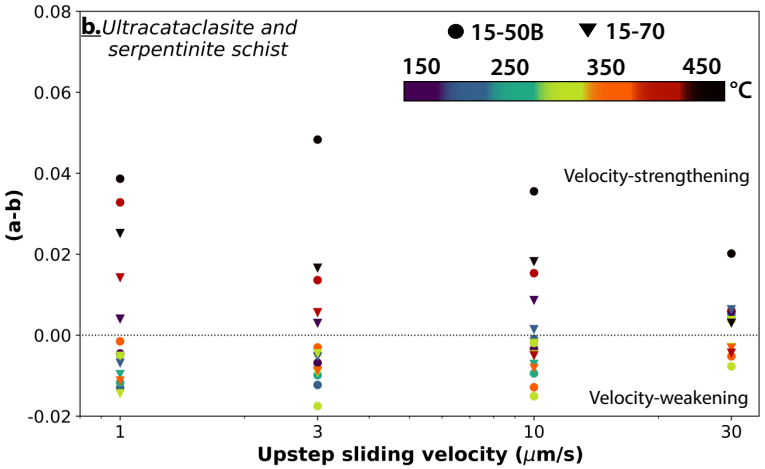
b. Ultracataclasite and serpentinite schist
15-50B
15-70
150 250 350 450 °C
Velocity-strengthening
Velocity-weakening
(a-b)
Upstep sliding velocity (μm/s)

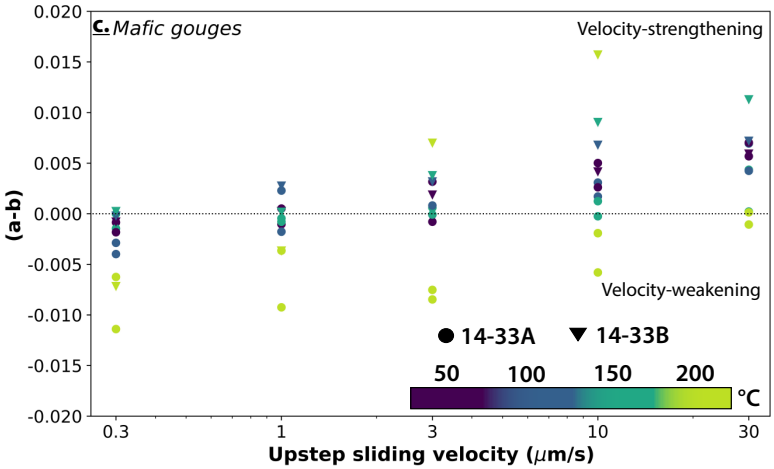
c. Mafic gouges
Velocity-strengthening
Velocity-weakening
14-33A
14-33B
50 100 150 200 °C
(a-b)
Upstep sliding velocity (μm/s)

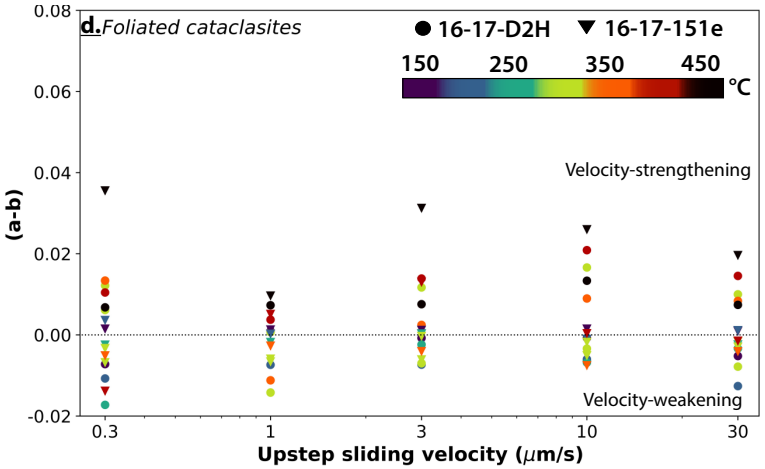
d. Foliated cataclasites
16-17-D2H
16-17-151e
150 250 350 450 °C
Velocity-strengthening
Velocity-weakening
(a-b)
Upstep sliding velocity (μm/s)

630

631 **Figure 7.** Rate-state-friction stability parameters *(a-b)* from velocity-stepping experiments on
632 Mai'iu fault rocks (Section 3.1, Figure 5, Table S6-7) including a.) corrensite-saponite gouges, b.)
633 ultracataclasite and serpentinite schist; c.) mafic gouges; d.) foliated cataclasites.
634

635 # 4. Discussion

636 ## 4.1. Experimental constraints on fault slip behavior

637 ### 4.1.1. Evidence for frictional strain-weakening of a rolling-hinge detachment

638 Our experimental results show that the Mai'iu fault gouges inferred to be active at the
639 shallowest depths are frictionally weak (μ = 0.11 – 0.35), with the most phyllosilicate-rich
640 (saponitic) gouge exhibiting the lowest static friction coefficients of 0.11 – 0.15. Saponite is
641 thermodynamically unstable above ~150 °C (e.g., Boulton et al., 2018; Moore, 2014), implying
642 that these weak gouges control the frictional strength of only the shallowest and most mechanically
643 misaligned portions of the Mai'iu fault, down to inferred depths of ~6 km (Figure 8; Mizera et al.,
644 submitted). At greater depths and higher temperatures (T = 150 – 225 and 150 – 300 °C,
645 respectively), chlorite thermometry from syntectonic structures (e.g., veins, shear bands) indicates
646 that slip occurred in the mafic ultracataclasite and foliated cataclasite units (Mizera et al.,
647 submitted), which are frictionally stronger (μ = 0.59 – 0.80 and μ = 0.44 – 0.75, respectively). This
648 increase in frictional strength with depth coincides with the depth range over which the fault dip
649 steepens from 15–22° in the upper 4–5 km to 30–40° below 5–6 km (Abers et al., 2016; Little et
650 al., 2019; Mizera et al., 2019; Webber et al., 2020). Based on these observations, we infer that the
651 static frictional strength of the Mai'iu fault partially controls its geometry, with slip at shallow dip
652 angles in the near-surface facilitated by abundant weak saponitic gouges, and slip at steeper dip
653 angles at greater depths occurring on frictionally stronger (ultra-)cataclasites, Formation of
654 saponite (or other weak phyllosilicate minerals in other LANFs) results in a syn-exhumational
655 reaction-weakening of the fault, consistent with classic geodynamic models of detachment faults
656 that require plastic strain-weakening of the normal fault zone in order for it to evolve into a long-
657 lived rolling hinge-style detachment (e.g., Lavier et al., 1999; 2000). Although this geodynamic
658 plastic strain-weakening is commonly modeled as a loss of cohesion (e.g., Lavier et al., 1999;
659 2000; Choi et al., 2012; Choi & Buck, 2013), our experimental results show that the effective
660 strain-weakening of an active rolling-hinge detachment fault (Mizera et al., 2019; Little et al.,
661 2019) can be at least partially accomplished by the reduction of the static coefficient of friction as

a result of fluid-assisted mineral transformation reactions that form weak phyllosilicate minerals such as saponite.

The static frictional strength of active LANFs is thought to influence both fault geometry according to classical Mohr-Coulomb-type fault mechanics (e.g., Axen, 2004; Choi & Buck, 2012; Choi et al., 2013; Collettini et al., 2009b; Collettini & Sibson, 2001; Yuan et al., 2020) and wedge geometry according to critical wedge theory and limit analysis (e.g., Yuan et al., 2020). The low frictional strength ($\mu \sim 0.2$) of clay-rich and/or hydrated gouge minerals such as talc and smectite should allow normal faults filled with these minerals to remain active at shallower dips (e.g., Collettini, 2011) and may resolve the apparent mechanical paradox of these anomalously low-angle structures. Although prior experimental friction studies of LANF zone rocks show some evidence of friction coefficients of 0.2 – 0.3 in the most phyllosilicate-rich or heavily foliated samples, many previously tested gouges show friction coefficients >0.4 (Collettini et al., 2009b; Haines et al., 2014; Smith & Faulkner, 2010; Niemeijer & Collettini, 2014; Numelin et al., 2007b). Our results confirm that shallow LANF gouges can be extremely frictionally weak, but suggest that LANF strength at greater depths depends on the frictional strength of the deeper fault rock protoliths of these gouges.

4.1.2. Depth-dependent frictional stability

One explanation for the paucity of recorded earthquakes on some LANFs is that they primarily creep aseismically (e.g., Abers, 2009; Hreinsdóttir & Bennett, 2009), implying that the fault material is predominantly velocity-strengthening through the brittle crust (e.g., Collettini, 2011). Indeed, velocity-stepping experiments on exhumed LANF gouges (Niemeijer & Colletini, 2013; Numelin et al., 2007b; Smith & Faulkner, 2010) and typical LANF gouge minerals (Collettini, 2011 and references within) show predominantly velocity-strengthening behavior under upper crustal conditions, with a thermally activated transition to velocity-weakening behavior at >300 °C (Niemeijer & Collettini, 2014).

Velocity-stepping experiments on Mai'iu fault sequence rocks ranging from mylonitic protoliths to well-developed gouges were performed under a range of temperature (50 – 450 °C), effective normal stress (30 – 210 MPa), and pore-fluid pressure (20 – 140 MPa) conditions associated with a range of crustal depths (~3 – 25 km, as inferred by Mizera et al., 2019). The saponite-rich gouges exhibit strictly velocity-strengthening behavior for temperatures <150 °C,

with the less-saponitic sample transitioning to velocity-weakening at T≥150 °C. In contrast, mild velocity-weakening behavior is observed for low upstep-velocities at T=50-200 °C in the mafic gouges, which contain less saponite (< 22%) and more remnant (ultra-)mafic clasts, chlorite, actinolite and epidote. The mafic gouges transition to velocity-strengthening with increasing upstep-velocity. These results suggest that the Mai'iu fault likely creeps at T<150 °C (<~6 km depth), but that local fault stability depends on the proportion of saponite to mafic components in the gouge. The hydrological and thermochemical conditions that promote the formation and accumulation of saponite appear crucial to development of frictionally weak, velocity-strengthening behavior in the upper reaches of the fault zone.

The fault rocks active at greater depths (>~6 km, based on temperatures >150 °C from Mizera et al., submitted) are more strongly and consistently velocity-weakening than any of the shallowly formed gouges. The cataclasites and ultracataclasite samples show predominantly negative *(a–b)* values (-0.02 < *(a–b)* < 0) at 150-350 °C, transitioning to consistently positive *(a-b)* values (0 < *(a–b)* < 0.05) at ≥400 °C. This transition to velocity-strengthening behavior around T=400 °C corresponds to the conditions under which most chlorite and chlorite-actinolite gouges have been observed to be strongly velocity-strengthening (T ≥ 400 °C and σ_n^{eff} = P_f ≥ 100 MPa, Okamoto et al., 2019, 2020). We infer that deformation at depths greater than the ~400 °C isotherm (> ~20-25 km depth) occurs primarily by aseismic ductile creep in the mafic mineral assemblage (chlorite, actinolite) within the mylonitic shear zone.

Altogether, the experimental friction results outline three primary temperature-dependent stability regimes of the Mai'iu fault rock sequence: low-temperature (≤ 150 °C) velocity-strengthening, intermediate-temperature (150-350 °C) velocity-weakening, and high-temperature velocity-strengthening (400-450 °C). Because the driving velocity in our experiments (1 μm/s) is orders of magnitude faster than natural tectonic plate rates, the frictional stability transitions observed in each rock type may shift to somewhat lower temperatures at slower deformation rates, as predicted by microphysical models (e.g., Chen et al., 2017 and references therein). In addition, laboratory experiments and geological mapping cannot constrain the size and spatial distribution of frictionally locked patches, which are determined by a variety of factors including the spatial distribution of different fault rocks and gouge minerals, local thermal structure, fault roughness and architectural complexity, presence and distribution of pore fluids, and local history and

heterogeneity of stress and slip on the fault, among others (e.g., Avouac, 2015; Burgmann, 2018; Harris, 2017; Scholz, 2019; references within).

4.2. Contemporary slip behavior in the context of geological and experimental evidence

GPS velocities near the active Mai'iu LANF reveal ~8 mm/yr of horizontal extension corresponding to ~10 mm/yr dip-slip on a normal fault dipping 26-35°. Horizontal velocities are fit similarly well by ~10 mm/yr of dip-slip with distinctly different distributions of interseismic fault locking: 1) aseismic creep below a shallowly locked patch (~2 km deep) that projects to the surface at the main fault trace; or 2) aseismic creep updip and downdip of a deeper locked patch (locked from ~5-16 km depth) that projects to the surface along a splay fault within the hanging-wall. We evaluate these two scenarios with respect to the experimental friction results alongside geological and geophysical evidence of Mai'iu fault slip.

The strongly velocity-strengthening behavior of the shallowest saponitic Mai'iu fault gouges (Figure 7a) suggests frictionally stable creep near the surface, while the predominantly velocity-weakening behavior of the cataclastic fault units deformed at greater depths (Figures 7b,d) points to deeper seismic slip and interseismic locking. The largely velocity-weakening behavior of the cataclasites and ultracataclasites from T=150-350 °C implies that frictional fault slip from ~8-20 km depth likely occurs as seismic or microseismic events that release elastic strain accumulated around frictionally locked patches. Along with evidence for sufficient seismic slip to generate pseudotachylite melts at 10-12 km depth (Little et al., 2019) and cause episodic meter-scale coastal uplifts further along-strike (Biemiller et al., 2018), these results are most consistent with model 2 (Figure 3d-f), which exhibits strong locking over the ~5-16 km depth range and would predict both earthquake nucleation and relatively uninhibited earthquake propagation through frictionally unstable velocity-weakening fault rocks (Figures 6-8). Model 1, by contrast, predicts aseismic creep below 2 km depth and negligible seismogenic potential at the depths of pseudotachylite formation and velocity weakening fault rocks. Although seismic rupture nucleated elsewhere could potentially propagate through a creeping segment to generate pseudotachylites, the depth-dependent stratification of fault slip stability illustrated by experimental friction and microstructural evidence implies deeper, stronger locking most consistent with model 2.

Frequent and localized microseismicity is common along actively creeping fault segments (e.g., Burgmann et al., 2000; Harris, 2017; Malservisi et al., 2005; Wolfson-Schwehr & Boettcher,

2019). Strongly aligned microseismicity from 12-25 km depth not only outlines the deeper extent of the Mai'iu fault, but also suggests that this portion of the fault zone actively creeps, generating microseismic events during frictional failure of small locked asperities within the creeping shear zone. The updip cutoff depth of this microseismicity around 12 km suggests a transition from steady creep below to stronger locking above, and may be associated with a transition from frictional-viscous velocity-strengthening creep to frictional velocity-weakening behavior around 10-15 km (Figure 8). Such depth-dependent mechanical transitions may be explained by our experimentally observed frictional transition from velocity-weakening to velocity-strengthening behavior in the cataclastic fault rocks at around 400 °C (Figures 6-7), as well as the microstructurally recorded mixed frictional-viscous deformation in the cataclasites and mylonites (Little et al., 2019; Mizera et al., submitted). The general depth range of this mechanical transition agrees well with model 2's predicted coupling transition from stronger locking around 5-16 km depth to creep downdip of this region; this coupling transition is not predicted by model 1 (Figures 3, 8). Combining our geodetic results with the diverse geological, experimental and seismological evidence for mixed seismic slip and aseismic creep, we infer that the Mai'iu fault is more strongly locked and potentially seismogenic from ~5-16 km depth and creeps both updip and downdip of this zone (model 2; Figure 8).

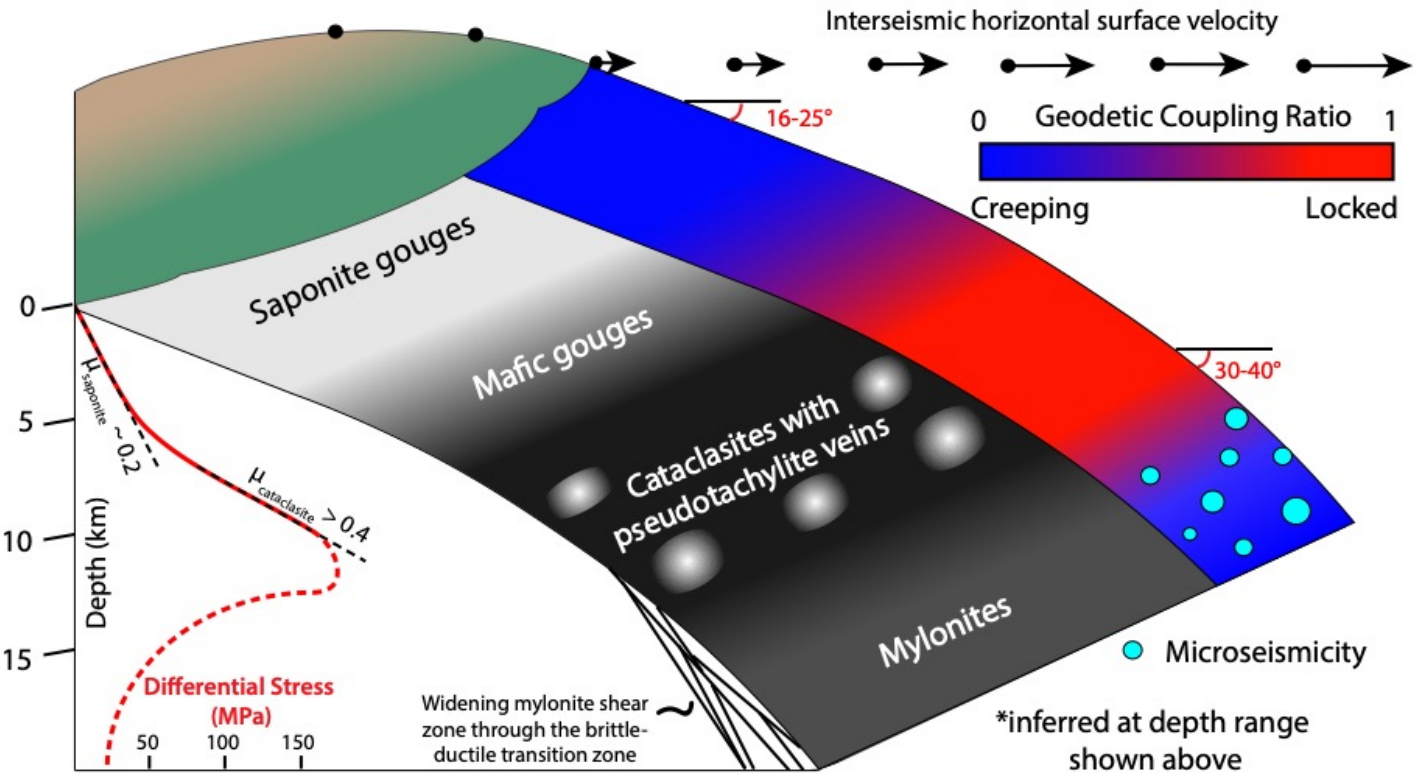

Fault Rock Unit	Friction Coefficient	Frictional Stability*	Deformation Mechanism*
Saponite gouges	0.11 - 0.28	Velocity-strengthening	Aseismic frictional creep
Mafic gouges	0.22 - 0.57	Velocity-weakening to velocity-strengthening	Mixed diffusion creep, frictional-viscous creep & seismic slip ('partial locking')
Cataclasites with pseudotachylite veins	0.44 - 0.80	Both velocity-weakening and velocity-strengthening	
Mylonites	0.6 - 0.8	Both velocity-weakening and velocity-strengthening	Diffusion creep, grain-boundary sliding, small frictional failures

Figure 8. Inferred distribution of active Mai'iu fault rocks and deformation mechanisms, along with the resulting geodetic coupling and horizontal surface velocities. Stronger locking occurs in the velocity-weakening cataclastic units, while stable interseismic creep occurs updip and downdip of this zone in the saponite gouges and mylonites, respectively. Frictional stability and strength derived from experiments (Figures 6-7) for all units except the mylonites, for which frictional behavior is inferred from microstructures (Little et al., 2019; Mizera et al., submitted) and microseismicity (Abers, 2016). The differential stress profile is based on frictional strength above the brittle-ductile transition zone (solid line) and is inferred only schematically below (dashed line).

4.3 Mechanical implications for LANFs

Active aseismic LANF creep below a shallow locking depth (model 1) would agree well with previous geodetic inferences of shallow aseismic creep on another active LANF, the Altotiberina fault (Hreinsdóttir & Bennett, 2009). However, allowing for more complex structures including creep and locking of nearby splay faults, subsequent modeling of the Altotiberina fault (Anderlini et al., 2016) has shown that a spatially heterogeneous pattern of locked and creeping patches is more consistent with observed surface GPS velocities. Similarly, based on the velocity-weakening frictional behavior of exhumed fault rocks, coseismically generated pseudotachylites exhumed from ~10–12 km depth, microseismicity data highlighting fault creep below ~12 km depth, and the results of geodetic models that allow for splay fault slip and patchy locking at depth, the Mai'iu fault appears to be more strongly locked from ~5–16 km depth (model 2) and to be creeping interseismically along its shallowest portions (<~5 km depth).

We suggest that the strongly coupled depth range of ~5-16 km corresponds to the brittle strength peak for the Mai'iu fault rock sequence where interseismic elastic strain can accumulate between periods of cataclastic deformation of potentially unstable velocity-weakening mylonitic protoliths (i.e., cataclasite and ultracataclasite units, Figures 5-7). With progressive slip and exhumation, fluid-assisted chemical reactions precipitate frictionally stable velocity-strengthening phyllosilicate gouge minerals (clays such as saponite; Figure 7a), responsible for the apparent transition towards aseismic creep near the surface. Models with deep locking below ~15 km do not fit the GPS data well (Figures 4, S4, S6); therefore, we infer that downdip of the strongly locked portion, slip occurs mostly by aseismic diffusive mass transfer creep processes, punctuated by microseismicity associated with occasional failure of small locked asperities and the fracturing of intact competent clasts within the primarily ductilely-deforming shear zone and also by the infrequent downdip propagation of large earthquake slip.

This interpretation of slip on the Mai'iu fault implies that it may be capable of hosting and even nucleating sizeable, albeit relatively infrequent, earthquakes. Assuming a typical dip-slip rupture width-length ratio of 0.668 (Leonard, 2010) and shear modulus of 25 GPa, nominal slip of 1 m on a locked patch dipping 35° from 5-16 km depth would correspond to a ~M_w 6.7 earthquake; allowing for rupture to the surface increases this estimate to ~M_w 7.0. These estimated magnitudes agree well with both the largest reported LANF earthquake globally (M_w 6.8, 29 October 1985; Abers, 2001; Abers et al., 1997) and estimations of Mai'iu fault earthquake magnitude based on

818 the stress and slip required for coseismic melting and pseudotachylite formation (M_w 6.0+; Little
819 et al., 2019). Taken together, these observations and calculations illustrate the potential severity of
820 Mai'iu fault earthquakes and the importance of including the Mai'iu fault and other active LANFs
821 in future seismic hazard assessments and risk mitigation plans.
822
823 **5.0 Conclusions**
824 New campaign GPS and experimental friction data from the Mai'iu fault in Papua New
825 Guinea illuminate the patterns and mechanisms of creep and locking on one of the world's fastest-
826 slipping, active low-angle normal faults. Horizontal GPS velocities indicate 8.3±1.2 mm/yr of
827 active extension across the Mai'iu fault. Friction experiments show that clay-rich gouges from the
828 shallowest and most poorly aligned portion of the fault are both weak (μ = 0.11-0.35) and
829 predominantly velocity-strengthening, while cataclastic fault rocks deformed at greater depths on
830 more steeply dipping parts of the fault are stronger (μ = 0.44-0.84) and predominantly velocity-
831 weakening. Two distinct fault locking models fit the GPS data equally well: one that requires
832 aseismic creep below ~2 km depth and one with a locked patch from ~5-16 km depth. A range of
833 geological, experimental, and seismological data support the geodetic model with interseismic
834 locking from ~5-16 km depth and shallower aseismic creep on the Mai'iu fault and one or more
835 hanging wall splay faults. This model also agrees with geological and coral paleoseismological
836 evidence of seismic slip on the Mai'iu fault and confirms that LANFs may be capable of hosting
837 M_w 7.0+ earthquakes despite the abundance of velocity-strengthening fault gouges at shallow
838 depths which promote interseismic creep near the Earth's surface.

839 **Acknowledgments & Data Availability**
840 We first and foremost thank the people of Milne Bay and Oro provinces in Papua New Guinea
841 for their support and hospitality, without which the field-based components would not have been
842 possible. We thank Samuel Webber, Neville Palmer, and Rory Hart for field and technical
843 support. We thank Samuel Webber, Jürgen Österle, Daniel Stockli, Kevin Norton, and Whitney
844 Behr for helpful discussions. This study was supported by the US National Science Foundation
845 grant EAR-1524729 (L.W., L.L, J.B.) and graduate student fellowship program (J.B.), New
846 Zealand Royal Society Marsden Fund grant VUW1310 (T.L., C.B., M.M., S.E.), European
847 Research Council grant SEISMIC (335915) (A.N.), and the Dutch Research Council VIDI grant
848 854.12.011 (A.N.).
849 Experimental friction data and GPS velocities are given in the Supporting Information.
850 GPS data are available through the UNAVCO data portal <link and DOI to be added>
851 Experimental friction data are available through the YODA online repository of the Utrecht
852 University (https://geo.yoda.uu.nl), as <link and DOI to be added>.
853

854 Abers, G. A., Eilon, Z., Gaherty, J. B., Jin, G., Kim, Y., Obrebski, M., & Dieck, C. (2016).
855 Southeast Papuan crustal tectonics: Imaging extension and buoyancy of an active rift.
856 *Journal of Geophysical Research: Solid Earth*, *121*(2), 951–971.
857 https://doi.org/10.1002/2015JB012621

858 Abers, G. a. (2001). Evidence for seismogenic normal faults at shallow dips in continental rifts.
859 *Geological Society, London, Special Publications*, *187*(1), 305–318.
860 https://doi.org/10.1144/GSL.SP.2001.187.01.15

861 Abers, G. A. (2009). Slip on shallow-dipping normal faults. *Geology*, *37*(8), 767–768.
862 https://doi.org/10.1130/focus082009.1.

863 Abers, G. A. (1991). Possible seismogenic shallow-dipping normal faults in the Woodlark-
864 D'Entrecasteaux extensional province, Papua New Guinea. *Geology*, *19*(12), 1205–1208.
865 https://doi.org/10.1130/0091-7613(1991)019<1205:pssdnf>2.3.co;2

866 Abers, G. A., Mutter, C. Z., & Fang, J. (1997). Shallow dips of normal faults during rapid
867 extension: Earthquakes in the Woodlark-D'Entrecasteaux rift system, Papua New Guinea.
868 *Journal of Geophysical Research: Solid Earth*, *102*(B7), 15301–15317.
869 https://doi.org/10.1029/97jb00787

870 Almeida, R., Lindsey, E. O., Bradley, K., Hubbard, J., Mallick, R., & Hill, E. M. (2018). Can the
871 Updip Limit of Frictional Locking on Megathrusts Be Detected Geodetically? Quantifying
872 the Effect of Stress Shadows on Near-Trench Coupling. *Geophysical Research Letters*,
873 *45*(10), 4754–4763. https://doi.org/10.1029/2018GL077785

874 Anderlini, L., Serpelloni, E., & Belardinelli, M. E. (2016). Creep and locking of a low-angle
875 normal fault: Insights from the Altotiberina fault in the Northern Apennines (Italy).
876 *Geophysical Research Letters*, *43*(9), 4321–4329. https://doi.org/10.1002/2016GL068604

877 Anzidei, M., Boschi, E., Cannelli, V., Devoti, R., Esposito, A., Galvani, A., … Serpelloni, E.
878 (2009). Coseismic deformation of the destructive April 6, 2009 L'Aquila earthquake
879 (central Italy) from GPS data. *Geophysical Research Letters*, *36*(17).
880 https://doi.org/10.1029/2009GL039145

881 Araki, E., Saffer, D. M., Kopf, A. J., Wallace, L. M., Kimura, T., Machida, Y., … Davis, E.
882 (2017). Recurring and triggered slow-slip events near the trench at the Nankai Trough
883 subduction megathrust. *Science*, *356*(6343), 1157–1160.
884 https://doi.org/10.1126/science.aan3120

885 Avouac, J.-P. (2015). From Geodetic Imaging of Seismic and Aseismic Fault Slip to Dynamic
886 Modeling of the Seismic Cycle. *Annual Review of Earth and Planetary Sciences*, *43*(1),
887 233–271. https://doi.org/10.1146/annurev-earth-060614-105302

888 Axen, G. J. (1992). Pore pressure, stress incraese, and fault weakening in low-angle normal
889 faulting. *Journal of Geophysical Research*, *97*(B6), 8979–8991.

Axen, G. J. (2004). Mechanics of Low-Angle Normal Faults. In *Rheology and Deformation of the Lithosphere at Continental Margins*. Columbia University Press. https://doi.org/10.7312/karn12738-004

Baldwin, S. L., Fitzgerald, P. G., & Webb, L. E. (2012). Tectonics of the New Guinea Region. *Annual Review of Earth and Planetary Sciences*, *40*(1), 495–520. https://doi.org/10.1146/annurev-earth-040809-152540

Banerjee, P., Pollitz, F. F., & Bürgmann, R. (2005). The Size and Duration of the Sumatra-Andaman Earthquake from Far-Field Static Offsets. *Science*, *308*(5729).

Beavan, J., Denys, P., Denham, M., Hager, B., Herring, T., & Molnar, P. (2010). Distribution of present-day vertical deformation across the Southern Alps, New Zealand, from 10 years of GPS data. *Geophysical Research Letters*, *37*(16), n/a-n/a. https://doi.org/10.1029/2010GL044165

Beavan, J., Moore, M., Pearson, C., Henderson, M., Parsons, B., Bourne, S., … Hodgkinson, K. (1999). Crustal deformation during 1994-1998 due to oblique continental collision in the central Southern Alps, New Zealand, and implications for seismic potential of the Alpine fault. *Journal of Geophysical Research: Solid Earth*, *104*(B11), 25233–25255. https://doi.org/10.1029/1999jb900198

Behnsen, J., & Faulkner, D. R. (2012). The effect of mineralogy and effective normal stress on frictional strength of sheet silicates. *Journal of Structural Geology*, *42*, 49–61. https://doi.org/10.1016/j.jsg.2012.06.015

Bennett, R. A., Hreinsdóttir, S., Velasco, M. S., & Fay, N. P. (2007). GPS constraints on vertical crustal motion in the northern Basin and Range. *Geophysical Research Letters*, *34*(22), L22319. https://doi.org/10.1029/2007GL031515

Biemiller, J., Wallace, L. M., Ellis, S. M., Little, T. A., Lavier, L., Mizera, M., … Webber, S. M. (2018). Short- and Long-term Deformation Styles on an Active Low-angle Normal Fault: Mai'iu Fault, Papua New Guinea. *AGUFM*, *2018*, T33D-0430.

Boulton, C., Barth, N. C., Moore, D. E., Lockner, D. A., Townend, J., & Faulkner, D. R. (2018). Frictional properties and 3-D stress analysis of the southern Alpine Fault, New Zealand. *Journal of Structural Geology*, *114*, 43–54. https://doi.org/10.1016/j.jsg.2018.06.003

Burgmann, R., Schmidt, D., Nadeau, R. M., d'Alessio, M., Fielding, E., Manaker, D., … Murray, M. H. (2000). Earthquake potential along the Northern Hayward fault, California. *Science*, *289*(5482), 1178–1182. https://doi.org/10.1126/science.289.5482.1178

Bürgmann, R. (2018). The geophysics, geology and mechanics of slow fault slip. *Earth and Planetary Science Letters*, *495*, 112–134. https://doi.org/10.1016/j.epsl.2018.04.062

924 Chen, J., Niemeijer, A. R., & Spiers, C. J. (2017). Microphysically Derived Expressions for
925 Rate-and-State Friction Parameters, a, b, and Dc. *Journal of Geophysical Research: Solid*
926 *Earth*, *122*(12), 9627–9657. https://doi.org/10.1002/2017JB014226

927 Chester, F. M., & Higgs, N. G. (1992). Multimechanism friction constitutive model for ultrafine
928 quartz gouge at hypocentral conditions. *Journal of Geophysical Research: Solid Earth*,
929 *97*(B2), 1859–1870. https://doi.org/10.1029/91JB02349

930 Chiaraluce, L., Chiarabba, C., Collettini, C., Piccinini, D., & Cocco, M. (2007). Architecture and
931 mechanics of an active low-angle normal fault: Alto Tiberina Fault, northern Apennines,
932 Italy. *Journal of Geophysical Research*, *112*(B10), B10310.
933 https://doi.org/10.1029/2007JB005015

934 Chiaraluce, L., Amato, A., Carannante, S., Castelli, V., Cattaneo, M., Cocco, M., … Valoroso, L.
935 (2014). The alto Tiberina near fault observatory (northern Apennines, Italy). *Annals of*
936 *Geophysics*, *57*(3). https://doi.org/10.4401/ag-6426

937 Choi, E., & Buck, W. R. (2012). Constraints on the strength of faults from the geometry of rider
938 blocks in continental and oceanic core complexes. *Journal of Geophysical Research: Solid*
939 *Earth*, *117*(B4), n/a-n/a. https://doi.org/10.1029/2011JB008741

940 Choi, E., Buck, W. R., Lavier, L. L., & Petersen, K. D. (2013). Using core complex geometry to
941 constrain fault strength. *Geophysical Research Letters*, *40*(15), 3863–3867.
942 https://doi.org/10.1002/grl.50732

943 Collettini, C., & Barchi, M. R. (2004). A comparison of structural data and seismic images for
944 low-angle normal faults in the Northern Apennines (Central Italy): Constraints on activity.
945 *Geological Society Special Publication*, *224*, 95–112.
946 https://doi.org/10.1144/GSL.SP.2004.224.01.07

947 Collettini, C., Tesei, T., Scuderi, M. M., Carpenter, B. M., & Viti, C. (2019). Beyond Byerlee
948 friction, weak faults and implications for slip behavior. *Earth and Planetary Science*
949 *Letters*, *519*, 245–263. https://doi.org/10.1016/j.epsl.2019.05.011

950 Collettini, C. (2011). The mechanical paradox of low-angle normal faults: Current understanding
951 and open questions. *Tectonophysics*, *510*(3–4), 253–268.
952 https://doi.org/10.1016/j.tecto.2011.07.015

953 Collettini, C., Niemeijer, A., Viti, C., & Marone, C. (2009b). Fault zone fabric and fault
954 weakness. *Nature*, *462*(7275), 907–910. https://doi.org/10.1038/nature08585

955 Collettini, C., & Sibson, R. H. (2001). Normal faults, normal friction? *Geology*, *29*(10), 927.
956 https://doi.org/10.1130/0091-7613(2001)029<0927:NFNF>2.0.CO;2

957 Collettini, C., Viti, C., Smith, S. A. F., & Holdsworth, R. E. (2009a). Development of
958 interconnected talc networks and weakening of continental low-angle normal faults.
959 *Geology*, *37*(6), 567–570. https://doi.org/10.1130/G25645A.1

960 Daczko, N. R., Caffi, P., Halpin, J. A., & Mann, P. (2009). Exhumation of the Dayman dome
961 metamorphic core complex, eastern Papua New Guinea. *Journal of Metamorphic Geology*,
962 *27*(6), 405–422. https://doi.org/10.1111/j.1525-1314.2009.00825.x

963 Dieterich, J. H. (1979). Modeling of rock friction: 1. Experimental results and constitutive
964 equations. *Journal of Geophysical Research*, *84*(B5), 2161.
965 https://doi.org/10.1029/JB084iB05p02161

966 Dieterich, J. H. (2013). Constitutive Properties of Faults With Simulated Gouge (pp. 103–120).
967 American Geophysical Union (AGU). https://doi.org/10.1029/gm024p0103

968 Duba, A. G., Durham, W. B., Handin, J. W., & Wang, H. F. (Eds.). (1990). *The Brittle-Ductile*
969 *Transition in Rocks* (Vol. 56). Washington, D. C.: American Geophysical Union.
970 https://doi.org/10.1029/GM056

971 Dziewonski, A. M., & Anderson, D. L. (1981). *Preliminary reference Earth model *.*
972 *Preliminary reference Earth modeL Phys. Earth Planet. Inter* (Vol. 25).

973 Floyd, J. S., Mutter, J. C., Goodliffe, A. M., & Taylor, B. (2001). Evidence for fault weakness
974 and fluid flow within an active low-angle normal fault. *Nature*, *411*(6839), 779–783.
975 https://doi.org/10.1038/35081040

976 Gu, J. C., Rice, J. R., Ruina, A. L., & Tse, S. T. (1984). Slip motion and stability of a single
977 degree of freedom elastic system with rate and state dependent friction. *Journal of the*
978 *Mechanics and Physics of Solids*, *32*(3), 167–196. https://doi.org/10.1016/0022-
979 5096(84)90007-3

980 Haines, S., Marone, C., & Saffer, D. (2014). Frictional properties of low-angle normal fault
981 gouges and implications for low-angle normal fault slip. *Earth and Planetary Science*
982 *Letters*, *408*, 57–65. https://doi.org/10.1016/j.epsl.2014.09.034

983 Harris, R. A. (2017, March 1). Large earthquakes and creeping faults. *Reviews of Geophysics*.
984 Blackwell Publishing Ltd. https://doi.org/10.1002/2016RG000539

985 Hayes, G. P. (2017). The finite, kinematic rupture properties of great-sized earthquakes since
986 1990. *Earth and Planetary Science Letters*, *468*, 94–100.
987 https://doi.org/10.1016/j.epsl.2017.04.003

988 He, C., Luo, L., Hao, Q.-M., & Zhou, Y. (2013). Velocity-weakening behavior of plagioclase
989 and pyroxene gouges and stabilizing effect of small amounts of quartz under hydrothermal
990 conditions. *Journal of Geophysical Research: Solid Earth*, *118*(7), 3408–3430.
991 https://doi.org/10.1002/jgrb.50280

992 Herring, T. A., Floyd, M. A., King, R. W., & McClusky, S. C. (2015). GLOBK Reference
993 Manual. Masschusetts Institute of Technology.

994 Herring, T. A., King, R. W.Floyd, M. A., & McClusky, S. C. (2018). GAMIT Reference Manual.
995 Masschusetts Institute of Technology.

996 Hreinsdóttir, S., & Bennett, R. A. (2009). Active aseismic creep on the Alto Tiberina low-angle
997 normal fault, Italy. *Geology*, *37*(8), 683–686. https://doi.org/10.1130/G30194A.1

998 Ikari, M. J., & Kopf, A. J. (2017). Seismic potential of weak, near-surface faults revealed at plate
999 tectonic slip rates. *Science Advances*, *3*(11), e1701269.
1000 https://doi.org/10.1126/sciadv.1701269

1001 Ikari, M. J., Marone, C., & Saffer, D. M. (2011). On the relation between fault strength and
1002 frictional stability. *Geology*, *39*(1), 83–86. https://doi.org/10.1130/G31416.1

1003 Ikari, M. J., Saffer, D. M., & Marone, C. (2009). Frictional and hydrologic properties of clay-rich
1004 fault gouge. *Journal of Geophysical Research: Solid Earth*, *114*(5).
1005 https://doi.org/10.1029/2008JB006089

1006 Jackson, J. A. (1987). Active normal faulting and crustal extension. *Geological Society Special*
1007 *Publication*, *28*, 3–17. https://doi.org/10.1144/GSL.SP.1987.028.01.02

1008 Jackson, J. A., & White, N. J. (1989). Normal faulting in the upper continental crust:
1009 observations from regions of active extension. *Journal of Structural Geology*, *11*(1–2), 15–
1010 36. https://doi.org/10.1016/0191-8141(89)90033-3

1011 Jackson, J., & McKenzie, D. (1983). The geometrical evolution of normal fault systems. *Journal*
1012 *of Structural Geology*, *5*(5), 471–482. https://doi.org/10.1016/0191-8141(83)90053-6

1013 Koulali, A., Tregoning, P., McClusky, S., Stanaway, R., Wallace, L., & Lister, G. (2015). New
1014 Insights into the present-day kinematics of the central and western Papua New Guinea from
1015 GPS. *Geophysical Journal International*, *202*(2), 993–1004.
1016 https://doi.org/10.1093/gji/ggv200

1017 Lavier, L. L., Buck, W. R., & Poliakov, A. (1999). Self-consistent rolling-hinge model for the
1018 evolution of large-onset low-angle normal faults. *Geology*, *27*(12), 1127–1130.
1019 https://doi.org/10.1130/0091-7613(1999)027<1127:SCRHMF>2.3.CO;2

1020 Lavier, L. L., Buck, W. R., & Poliakov, A. N. B. (2000). Factors controlling normal fault offset
1021 in an ideal brittle layer. *Journal of Geophysical Research: Solid Earth*, *105*(B10), 23431–
1022 23442. https://doi.org/10.1029/2000JB900108

1023 Lay, T., Ye, L., Ammon, C. J., & Kanamori, H. (2017). Intraslab rupture triggering megathrust
1024 rupture coseismically in the 17 December 2016 Solomon Islands M_w 7.9 earthquake.
1025 *Geophysical Research Letters*, *44*(3), 1286–1292. https://doi.org/10.1002/2017GL072539

1026 Lee, S., Lin, T., Feng, K., & Liu, T. (2018). Composite Megathrust Rupture From Deep
1027 Interplate to Trench of the 2016 Solomon Islands Earthquake. *Geophysical Research*
1028 *Letters*, *45*(2), 674–681. https://doi.org/10.1002/2017GL076347

1029 Leonard, M. (2010). Earthquake fault scaling: Self-consistent relating of rupture length, width,
1030 average displacement, and moment release. *Bulletin of the Seismological Society of*
1031 *America*, *100*(5 A), 1971–1988. https://doi.org/10.1785/0120090189

1032 Little, T. A., Hacker, B. R., Gordon, S. M., Baldwin, S. L., Fitzgerald, P. G., Ellis, S., &
1033 Korchinski, M. (2011). Diapiric exhumation of Earth's youngest (UHP) eclogites in the
1034 gneiss domes of the D'Entrecasteaux Islands, Papua New Guinea. *Tectonophysics*, *510*(1–
1035 2), 39–68. https://doi.org/10.1016/j.tecto.2011.06.006

1036 Little, T. A., Baldwin, S. L., Fitzgerald, P. G., & Monteleone, B. (2007). Continental rifting and
1037 metamorphic core complex formation ahead of the Woodlark spreading ridge,
1038 D'Entrecasteaux Islands, Papua New Guinea. *Tectonics*, *26*(1), 1–26.
1039 https://doi.org/10.1029/2005TC001911

1040 Little, T. A., Webber, S. M., Mizera, M., Boulton, C., Oesterle, J., Ellis, S., … Wallace, L.
1041 (2019). Evolution of a rapidly slipping, active low-angle normal fault, Suckling-Dayman
1042 metamorphic core complex, SE Papua New Guinea. *GSA Bulletin*.
1043 https://doi.org/10.1130/B35051.1

1044 Lockner, D. A., Morrow, C., Moore, D., & Hickman, S. (2011). Low strength of deep San
1045 Andreas fault gouge from SAFOD core. *Nature*, *472*(7341), 82–86.
1046 https://doi.org/10.1038/nature09927

1047 Malservisi, R., Furlong, K. P., & Gans, C. R. (2005). Microseismicity and creeping faults: Hints
1048 from modeling the Hayward fault, California (USA). *Earth and Planetary Science Letters*,
1049 *234*(3–4), 421–435. https://doi.org/10.1016/j.epsl.2005.02.039

1050 Mann, P., Horton, B. K., Taylor, F. W., Shen, C., Lin, K., Renema, W., … Renema, W. (2009).
1051 Uplift patterns of reef terraces and sedimentary rocks constrain tectonic models for
1052 metamorphic core complexes in eastern Papua New Guinea. *AGUFM*, *2009*, G33B-0642.

1053 Mann, P., & Taylor, F. W. (2002). Emergent Late Quaternary Coral Reefs of Eastern Papua New
1054 Guinea Constrain the Regional Pattern of Oceanic Ridge Propagation. *AGUFM*, *2002*,
1055 T52C-1206.

1056 Marone, C. (1998). LABORATORY-DERIVED FRICTION LAWS AND THEIR
1057 APPLICATION TO SEISMIC FAULTING. *Annual Review of Earth and Planetary*
1058 *Sciences*, *26*(1), 643–696. https://doi.org/10.1146/annurev.earth.26.1.643

1059 Mccaffrey, R. (2013). Crustal Block Rotations and Plate Coupling (pp. 101–122). American
1060 Geophysical Union (AGU). https://doi.org/10.1029/gd030p0101

1061 Mizera, M., Little, T. A., Biemiller, J., Ellis, S., Webber, S., & Norton, K. P. (2019). Structural
1062 and Geomorphic Evidence for Rolling-Hinge Style Deformation of an Active Continental
1063 Low-Angle Normal Fault, SE Papua New Guinea. *Tectonics*, *38*(5), 1556–1583.
1064 https://doi.org/10.1029/2018TC005167

1065 Moore, D. E. (2014). Comparative mineral chemistry and textures of SAFOD fault gouge and
1066 damage-zone rocks. *Journal of Structural Geology*, *68*(PA), 82–96.
1067 https://doi.org/10.1016/j.jsg.2014.09.002

1068 Niemeijer, A. R., Boulton, C., Toy, V. G., Townend, J., & Sutherland, R. (2016). Large-
1069 displacement, hydrothermal frictional properties of DFDP-1 fault rocks, Alpine Fault, New
1070 Zealand: Implications for deep rupture propagation. *Journal of Geophysical Research: Solid*
1071 *Earth*, *121*(2), 624–647. https://doi.org/10.1002/2015JB012593

1072 Niemeijer, A. R., Boulton, C., Toy, V. G., Townend, J., & Sutherland, R. (2016). Large-
1073 displacement, hydrothermal frictional properties of DFDP-1 fault rocks, Alpine Fault, New
1074 Zealand: Implications for deep rupture propagation. *Journal of Geophysical Research: Solid*
1075 *Earth*, *121*(2), 624–647. https://doi.org/10.1002/2015JB012593

1076 Niemeijer, A. R., & Collettini, C. (2014). Frictional Properties of a Low-Angle Normal Fault
1077 Under In Situ Conditions: Thermally-Activated Velocity Weakening. *Pure and Applied*
1078 *Geophysics*, *171*(10), 2641–2664. https://doi.org/10.1007/s00024-013-0759-6

1079 Numelin, T., Marone, C., & Kirby, E. (2007b). Frictional properties of natural fault gouge from a
1080 low-angle normal fault, Panamint Valley, California. *Tectonics*, *26*(2), n/a-n/a.
1081 https://doi.org/10.1029/2005TC001916

1082 Numelin, T., Kirby, E., Walker, J. D., & Didericksen, B. (2007a). Late Pleistocene slip on a low-
1083 angle normal fault, Searles Valley, California. *Geosphere*, *3*(3), 163–176.
1084 https://doi.org/10.1130/GES00052.1

1085 Okada, Y. (1985). Surface deformation due to shear and tensile faults in a half-space. *Bulletin of*
1086 *the Seismological Society of America*, *75*(4), 1135–1154.

1087 Okamoto, A. S., Niemeijer, A. R., Takeshita, T., Verberne, B. A., & Spiers, C. J. (2020).
1088 Frictional properties of actinolite-chlorite gouge at hydrothermal conditions.
1089 *Tectonophysics*, *779*, 228377. https://doi.org/10.1016/j.tecto.2020.228377

1090 Okamoto, A. S., Verberne, B. A., Niemeijer, A. R., Takahashi, M., Shimizu, I., Ueda, T., &
1091 Spiers, C. J. (2019). Frictional Properties of Simulated Chlorite Gouge at Hydrothermal
1092 Conditions: Implications for Subduction Megathrusts. *Journal of Geophysical Research:*
1093 *Solid Earth*, *124*(5), 4545–4565. https://doi.org/10.1029/2018JB017205

1094 Österle, J. E., Little, T. A., Seward, D., Stockli, D. F., & Gamble, J. (2020). The petrology,
1095 geochronology and tectono-magmatic setting of igneous rocks in the Suckling-Dayman

metamorphic core complex, Papua New Guinea. *Gondwana Research*. https://doi.org/10.1016/j.gr.2020.01.014

Platt, J. P., Behr, W. M., & Cooper, F. J. (2015). Metamorphic core complexes: windows into the mechanics and rheology of the crust. *Journal of the Geological Society*, *172*(1), 9–27. https://doi.org/10.1144/jgs2014-036

Pollitz, F. F. (1996). Coseismic Deformation From Earthquake Faulting On A Layered Spherical Earth. *Geophysical Journal International*, *125*(1), 1–14. https://doi.org/10.1111/j.1365-246X.1996.tb06530.x

Reinen, L. A., & Weeks, J. D. (1993). Determination of rock friction constitutive parameters using an iterative least squares inversion method. *Journal of Geophysical Research*, *98*(B9), 15937–15950. https://doi.org/10.1029/93jb00780

Rice, J. R., & Tse, S. T. (1986). Dynamic motion of a single degree of freedom system following a rate and state dependent friction law. *Journal of Geophysical Research*, *91*(B1), 521. https://doi.org/10.1029/JB091iB01p00521

Ross, J. V., & Lewis, P. D. (1989). Brittle-ductile transition: semi-brittle behavior. *Tectonophysics*, *167*(1), 75–79. https://doi.org/10.1016/0040-1951(89)90295-3

Ruina, A. (1983). Slip instability and state variable friction laws. *Journal of Geophysical Research: Solid Earth*, *88*(B12), 10359–10370. https://doi.org/10.1029/JB088iB12p10359

Ruppel, C. (1995). Extensional processes in continental lithosphere. *Journal of Geophysical Research*, *100*(B12). https://doi.org/10.1029/95jb02955

Scholz, C. H. (2019). *The Mechanics of Earthquakes and Faulting* (3rd ed.). Cambridge: Cambridge University Press. https://doi.org/DOI: 10.1017/9781316681473

Serpelloni, E., Faccenna, C., Spada, G., Dong, D., & Williams, S. D. P. (2013). Vertical GPS ground motion rates in the Euro-Mediterranean region: New evidence of velocity gradients at different spatial scales along the Nubia-Eurasia plate boundary. *Journal of Geophysical Research: Solid Earth*, *118*(11), 6003–6024. https://doi.org/10.1002/2013JB010102

Smith, I. E., & Davies, H. L. (1976). *Geology of the Southeast Papuan Mainland*. Canberra: Australian Government Publishing Service for the Bureau of Mineral Resources, Geology and Geophysics.

Smith, S. A. F., & Faulkner, D. R. (2010). Laboratory measurements of the frictional properties of the Zuccale low-angle normal fault, Elba Island, Italy. *Journal of Geophysical Research: Solid Earth*, *115*(2). https://doi.org/10.1029/2008JB006274

Sone, H., Shimamoto, T., & Moore, D. E. (2012). Frictional properties of saponite-rich gouge from a serpentinite-bearing fault zone along the Gokasho-Arashima Tectonic Line, central

Japan. *Journal of Structural Geology*, *38*, 172–182. https://doi.org/10.1016/j.jsg.2011.09.007

Strasser, F. O., Arango, M. C., & Bommer, J. J. (2010). Scaling of the source dimensions of interface and intraslab subduction-zone earthquakes with moment magnitude. *Seismological Research Letters*, *81*(6), 941–950. https://doi.org/10.1785/gssrl.81.6.941

Taylor, B., Goodliffe, A. M., & Martinez, F. (1999). How continents break up: Insights from Papua New Guinea. *Journal of Geophysical Research: Solid Earth*, *104*(B4), 7497–7512. https://doi.org/10.1029/1998jb900115

Taylor, F. W., Briggs, R. W., Frohlich, C., Brown, A., Hornbach, M., Papabatu, A. K., … Billy, D. (2008). Rupture across arc segment and plate boundaries in the 1 April 2007 Solomons earthquake. *Nature Geoscience*, *1*(4), 253–257. https://doi.org/10.1038/ngeo159

Tregoning, P., Burgette, R., McClusky, S. C., Lejeune, S., Watson, C. S., & McQueen, H. (2013). A decade of horizontal deformation from great earthquakes. *Journal of Geophysical Research: Solid Earth*, *118*(5), 2371–2381. https://doi.org/10.1002/jgrb.50154

Tullis, J., & Yund, R. A. (1987). Transition from cataclastic flow to dislocation creep of feldspar. *Geology*, *15*(001), 606–609. https://doi.org/10.1130/0091-7613(1987)15<606:TFCFTD>2.0.CO

U.S. Geological Survey. (2019). Earthquake Hazards Program.

Valoroso, L., Chiaraluce, L., Di Stefano, R., & Monachesi, G. (2017). Mixed-Mode Slip Behavior of the Altotiberina Low-Angle Normal Fault System (Northern Apennines, Italy) through High-Resolution Earthquake Locations and Repeating Events. *Journal of Geophysical Research: Solid Earth*, *122*(12), 10,220-10,240. https://doi.org/10.1002/2017JB014607

Wallace, L. M., Taylor, F. W., Bevis, M. G., Phillips, D. A., Walter, J. I., Kendrick, E. C., … Papabatu, A. K. (2015). Interseismic, coseismic, postseismic, and slow slip event deformation above a shallow subduction thrust in the western Solomon Islands. *AGUFM*, *2015*, T44B-07.

Wallace, L. M., Ellis, S., Little, T., Tregoning, P., Palmer, N., Rosa, R., … Kwazi, J. (2014). Continental breakup and UHP rock exhumation in action: GPS results from the Woodlark Rift, Papua New Guinea. *Geochemistry, Geophysics, Geosystems*, *15*(11), 4267–4290. https://doi.org/10.1002/2014GC005458

Warren, J. M., & Hirth, G. (2006). Grain size sensitive deformation mechanisms in naturally deformed peridotites. *Earth and Planetary Science Letters*, *248*(1–2), 438–450. https://doi.org/10.1016/j.epsl.2006.06.006

1164 Webber, S., Little, T. A., Norton, K. P., Österle, J., Mizera, M., Seward, D., & Holden, G.
1165 (2020). Progressive back-warping of a rider block atop an actively exhuming, continental
1166 low-angle normal fault. *Journal of Structural Geology*, *130*, 103906.
1167 https://doi.org/10.1016/j.jsg.2019.103906

1168 Webber, S., Norton, K. P., Little, T. A., Wallace, L. M., & Ellis, S. (2018). How fast can low-
1169 angle normal faults slip? Insights from cosmogenic exposure dating of the active Mai'iu
1170 fault, Papua New Guinea. *Geology*, *46*(3), 227–230. https://doi.org/10.1130/G39736.1

1171 Wernicke, B. (1995). Low-angle normal faults and seismicity: A review. *Journal of Geophysical*
1172 *Research: Solid Earth*, *100*(B10), 20159–20174. https://doi.org/10.1029/95JB01911

1173 Williams, S. D. P., Bock, Y., Fang, P., Jamason, P., Nikoladi, R., Prawirodirdjo, L., … Johnson,
1174 D. (2004). Error analysis of continuous GPS position time series. *Journal of Geophysical*
1175 *Research*, *109*(B3). https://doi.org/10.1029/2003jb002741

1176 Wolfson-Schwehr, M., & Boettcher, M. S. (2019). Global Characteristics of Oceanic Transform
1177 Fault Structure and Seismicity. In *Transform Plate Boundaries and Fracture Zones* (pp. 21–
1178 59). Elsevier. https://doi.org/10.1016/b978-0-12-812064-4.00002-5

1179 Zhang, J., Bock, Y., Johnson, H., Fang, P., Williams, S., Genrich, J., … Behr, J. (1997).
1180 Southern California permanent GPS geodetic array: Error analysis of daily position
1181 estimates and site velocities. *Journal of Geophysical Research: Solid Earth*, *102*(B8),
1182 18035–18055. https://doi.org/10.1029/97jb01380